Defense Threat Reduction Agency
8725 John J. Kingman Road, MS-6201
Fort Belvoir, VA 22060-6201

TECHNICAL REPORT

Meso-Scale Experimental & Numerical Studies for Predicting Macro-scale Performance of Advanced Reactive Materials (ARMs)

Distribution Statement A. Approved for public release; distribution is unlimited.

April 2015

Naresh Thadhani et al.

Prepared by:
Georgia Tech Research Corporation
School of Materials Science and Engineering
771 Ferst Drive
Atlanta, GA 30332

DESTRUCTION NOTICE:

REPORT DOCUMENTATION PAGE

Form Approved
OMB No. 0704-0188

Public reporting burden for this collection of information is estimated to average 1 hour per response, including the time for reviewing instructions, searching existing data sources, gathering and maintaining the data needed, and completing and reviewing this collection of information. Send comments regarding this burden estimate or any other aspect of this collection of information, including suggestions for reducing this burden to Department of Defense, Washington Headquarters Services, Directorate for Information Operations and Reports (0704-0188), 1215 Jefferson Davis Highway, Suite 1204, Arlington, VA 22202-4302. Respondents should be aware that notwithstanding any other provision of law, no person shall be subject to any penalty for failing to comply with a collection of information if it does not display a currently valid OMB control number. **PLEASE DO NOT RETURN YOUR FORM TO THE ABOVE ADDRESS.**

1. REPORT DATE *(DD-MM-YYYY)*	2. REPORT TYPE	3. DATES COVERED *(From - To)*
00-04-2015	Technical	January 3, 2010 - February 28, 2014

4. TITLE AND SUBTITLE	5a. CONTRACT NUMBER
Meso-Scale Experimental & Numerical Studies For Predicting Macro-Scale Performance of Advanced Reactive Materials	HDTRA1-10-1-0038
	5b. GRANT NUMBER
	5c. PROGRAM ELEMENT NUMBER

6. AUTHOR(S)	5d. PROJECT NUMBER
Naresh Thadhani, Arun Gokhale, Jason Quenneville, Jennifer Breidenich, Manny Gonzales, and Ashok Gurumurthy	
	5e. TASK NUMBER
	5f. WORK UNIT NUMBER

7. PERFORMING ORGANIZATION NAME(S) AND ADDRESS(ES)	8. PERFORMING ORGANIZATION REPORT NUMBER
Georgia Tech Research Corp School of Materials Science and Engineering 771 Ferst Drive Atlanta, GA 30332	

9. SPONSORING / MONITORING AGENCY NAME(S) AND ADDRESS(ES)	10. SPONSOR/MONITOR'S ACRONYM(S)
Defense Threat Reduction Agency 8725 John J. Kingman Road STOP 6201 Fort Belvoir, VA 22060 PM/Suhithi Peiris	DTRA
	11. SPONSOR/MONITOR'S REPORT NUMBER(S) DTRA-TR-14-49

12. DISTRIBUTION / AVAILABILITY STATEMENT

Distribution Statement A. Approved for public release; distribution is unlimited.

13. SUPPLEMENTARY NOTES

14. ABSTRACT

Our collaborative, multi-disciplinary and multi-investigator research project, combines numerical simulations with time-resolved impact experiments, to determine the meso-scale mechanisms of impact-initiated reactions in Ti-Al-B based reactive materials in the form of compacts of powders of different sizes and morphologies. The major goal is to delineate how processes of localized deformation and flow, or fracture and fragmentation, create the dispersion and mixing of reactants and provide the thermal and mass transport resulting in highly exothermic Ti and B intermetallic reaction and/or oxidation reaction (Al or B). The time sequence of events associated with reaction initiation as well as subsequent interactions with the external environment are also being determined. More specifically, the influence of material-inherent elastic/plastic properties and reactant configuration (e.g., porosity, morphology, spacing, distribution, etc., created from a library of microstructures) on meso-scale mechanistic processes and the resulting macro-scale performance is being established.

15. SUBJECT TERMS

reactive materials   shock compression   high-strain-rate deformation   meso-scale computations

16. SECURITY CLASSIFICATION OF:			17. LIMITATION OF ABSTRACT	18. NUMBER OF PAGES	19a. NAME OF RESPONSIBLE PERSON Suhithi Peiris
a. REPORT	**b. ABSTRACT**	**c. THIS PAGE**	SAR	54	**19b. TELEPHONE NUMBER** *(include area code)*
Unclassified	Unclassified	Unclassified			703-767-4732

Standard Form 298 (Rev. 8-98)
Prescribed by ANSI Std. Z39.18

MESO-SCALE EXPERIMENTAL & NUMERICAL STUDIES FOR PREDICTING MACRO-SCALE PERFORMANCE OF ADVANCED REACTIVE MATERIALS (ARMS)

Jennifer Breidenich, Arun Gokhale, Manny Gonzales, Ashok Gurumurthy, and Naresh Thadhani

School of Materials Science and Engineering, Georgia Institute of Technology

and

Jason Quenneville
Spectral Sciences Inc., Spectral Sciences Inc., Burlington,MA 01803

P.I. Name: Naresh Thadhani
Organization: Georgia Tech Research Corporation
Address: School of Materials Science and Engineering, Georgia Institute of Technology, 771 Ferst Drive, Atlanta, GA 30332-0245

Final Report

April 28, 2014

TABLE OF CONTENTS

Grant/Award #: HDTRA1-10-1-0038
PI Name: Naresh Thadhani
Organization: Georgia Institute of Technology
Project Title: Meso-scale Experimental & Numerical Studies for Predicting Macro-scale Performance of Advanced Reactive Materials (ARMs)

ABSTRACT

Our collaborative, multi-disciplinary and multi-investigator research project, combines numerical simulations with time-resolved impact experiments, to determine the meso-scale mechanisms of impact-initiated reactions in Ti-Al-B based reactive materials in the form of compacts of powders of different sizes and morphologies. The major goal is to delineate how processes of localized deformation and flow, or fracture and fragmentation, create the dispersion and mixing of reactants and provide the thermal and mass transport resulting in highly exothermic Ti and B intermetallic reaction and/or oxidation reaction (Al or B). The time sequence of events associated with reaction initiation as well as subsequent interactions with the external environment are also being determined. More specifically, the influence of material-inherent elastic/plastic properties and reactant configuration (e.g., porosity, morphology, spacing, distribution, etc., created from a library of microstructures) on meso-scale mechanistic processes and the resulting macro-scale performance is being established. The combination of experiments and numerical simulations that capture morphologies of real materials through the creation of synthetic microstructures from a library of constituent morphologies is used to correlate processes across various length scales and predict fundamental spatial and temporal understanding of meso-scale intermetallic and/or oxidation reaction processes. The fundamental predictive studies have the potential to enable designs of the meso-scale structure of advanced reactive materials.

1.   INTRODUCTION

The research performed in this work was aimed at generating the fundamental *spatial* and *temporal* understanding of the meso-scale mechanisms of impact-initiated anaerobic chemical reactions in intermetallic-based reactive materials in the form of nano/micro-sized particulate compacts and layered structures. The specific objectives of the proposed work are to (a) delineate how processes of localized deformation and flow, or fracture and fragmentation, create the dispersion and mixing of reactants and provide the thermal and mass transport needed for anaerobic chemical reaction initiation; (b) determine the time sequence of events associated with reaction initiation, as well as subsequent interactions with external environment; and (c) establish the role of material-inherent elastic/plastic properties and reactant configuration (e.g., porosity, morphology, distribution, etc.) on the mechanisms and kinetics of meso-scale processes and the resulting macro-scale energetic performance of such anaerobic reactions. These objectives have been pursued through four distinct activities,

4

integrated to generate a predictive understanding of the meso-scale mechanisms of impact-initiated reactions in Ti-Al-B based reactive materials.

2. BACKGROUND

2.1 Characteristics of Anaerobic Reactions

The energy release characteristics of intermetallic-forming reactive materials combined with their mechanical properties makes them highly desirable in defense weapons applications.[1] Reactive materials are inherently heterogeneous, with meso-scale variations in nano- to micro-meter size of reactants of various forms/morphologies. Shock initiation of reactions is dominated by physical, mechanical, and chemical processes that occur in the nanosecond time-scale of the rise to the peak pressure, to the tens of microsecond time scale of temperature equilibration.[2] Understanding the influence of meso-scale spatial variations and probing processes in real time is essential for predicting the macro-scale reaction response. Time-resolved experiments employing conventional diagnostics provide nanosecond temporal resolution, yet there is a limit to the type of information obtained. Hence, observations of indirect inference of reaction have often been utilized based on expanded P-V compressibility states[3] or increased shock speeds.[4]

Details of meso-scale processes in reactant particles are often investigated through computations. Discrete-element computations[5] have provided an excellent parametric study of the influence of internal void content, strain-rate, relative yield strength, and melting on the degree of mixing and reactions in regions of highly localized deformation (or shear-bands). The results have revealed an optimum strength ratio between components of most effective inter-reactant mixing, the extent of which increases with shear strain-rate. Melting occurring more rapidly at high strain-rates, leads to loss of strength, and increases strength ratio, producing a negative effect on mass mixing such that the chemical reaction is hindered. Computations[6] with simulated (2-D) microstructures have been used to describe the evolution of reactant and product configurations following shock compression. Computations with 3-D simulated microstructures have also been performed.[7] However, similar to the discrete element method, these computations have employed idealized reactant geometries (spherical, cubic, angular) and their distributions, which are disadvantaged in the case where the characteristics of heterogeneities are far from ideal, and where variations exist across different length scales, particularly if the goal is to perform predictive modeling of macro-scale performance.

2.2 Configurational Effects on Anaerobic Chemical Reactions

Intermetallic-based reactive materials are non-explosive and non-detonable, but can rapidly release large amounts of the anaerobic heat of reaction.[8] While processes of thermal ignition in such reactive materials are well understood,[9] the mechanisms of impact-initiated reactions and their kinetics remain to be established. Our prior work[10,11,12] showed that ***shock-initiation*** of chemical reactions is influenced by differences in the elastic/plastic properties of reactant materials and their morphological characteristics. Under uniaxial-strain loading, micro-

size spherical Ni+Al powder mixtures showed crush-up to full density at ~0.5 GPa, while the crush-up stress for flake-Ni+Al mixtures of similar size is ~2 GPa, and that of nano-sized Ni+Al was ~6 GPa.[13] However, flake-Ni+Al mixtures reacted at the lowest threshold stress, due to the additional bending and buckling modes that cause the flake-Ni particles to undergo the same degree of plastic deformation as the lower strength Al particles, thereby promoting mixing and consequent reaction initiation. Likewise, Ti and Si powder mixtures have shown variable reactivity as a function of size, dictated by the ability of the covalently bonded Si particles to undergo deformation or fracture.[8] Barring the fine (<2 μm) powders which tend to agglomerate, Si particles of 10-20 μm size undergo plastic deformation simultaneously with the Ti particles of the same size, while coarse Si particles (>100 μm) fracture and become entrapped within the deformed Ti. Lack of flow of Si particles due to agglomeration, or fracture and entrapment, restricts mixing and subsequent reaction, while simultaneous deformation and flow of Si with Ti, promotes mixing and subsequent mechanochemical reaction at a threshold *shock-pressure* of ~1 GPa. A threshold *shock-energy*[14] criterion for reaction initiation has also been postulated for Ti+Si mixtures with varying porosity levels. The energy threshold corresponds to the work of shock compression leading to a mean equilibrated (bulk) temperature rise exceeding that needed for thermally-initiated reaction. However, the temperature equilibration time-scale (tens of microseconds to milliseconds) significantly exceeds the shock-pulse duration. Hence, the threshold *shock-energy* criterion is applicable to <u>shock-assisted</u> thermochemical reactions occurring after unloading, and contrasting with <u>shock-induced</u> mechanochemical reactions that occur during the shock state.[2]

The varied mechanical and chemical responses described above are controlled by meso-scale processes, which in turn are influenced by (a) stress states and pressure/temperature histories generated due to the macro-scale geometry, impact configuration, and loading conditions, (b) variations in inter-reactant contact areas and local stress/strain distributions caused by morphological form (shape, size, distribution) of reactants, and (c) inherent differences in elastic and plastic properties of reactants. Probing of meso-scale processes is therefore, essential for developing a complete understanding of the mechanisms and kinetics of anaerobic reactions and the energy release characteristics of reactive materials. The understanding generated can allow correlation of the macro-scale performance (in terms of the extent of reaction and associated temperature and pressure changes) with the structure, and also make it possible to reverse design the reactants architecture for desired macro-scale properties and performance characteristics.

2.3   Characteristic Scales for Defining Meso-scale Processes

Probing *meso-scale processes* in a macroscopic bulk reactive material requires defining a *representative volume element (RVE)* that it is large enough to capture the spatial scales, distributions, and morphological features of reactants. The RVE however, can be quite different for nanometer or micrometer size reactant particles/grains/layers/laminates. As illustrated in Fig. 1, the description of meso-scale processes for an RVE also requires defining the stress-state and strain-rate bounds from the higher level associated with **macro-scale** sample geometry/configuration, and likewise the lower level local stress-strain distributions, processes

6

Fig.1. Relevant length scales in macroscopic reactive material.
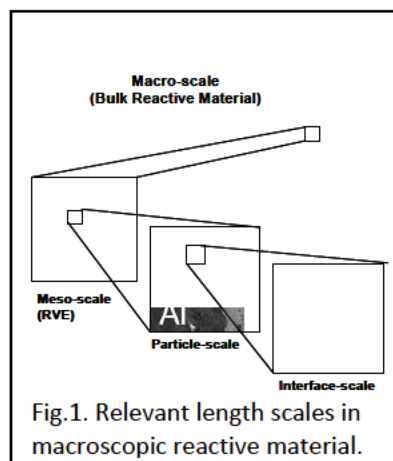
of plastic flow and/or fracture, mixing/transport of reactants occurring at the **particle-scale,** as well as the **interface-scale.** Use of real imported microstructures enables such a linkage by providing a realistic representation of the size and form of the constituents. It also makes it possible to probe and correlate processes across the length scales. The use of imported microstructures to describe the response of materials has been used to address a wide variety of materials applications, including predictions of: (a) 3-D fluid flow and permeability in asphalt pavements,[15] (b) thermal conductivity of thermal barrier coatings,[16] (c) dynamics of fracture path and crack propagation in Al+SiC composites[17] and TiB_2+Al_2O_3 two-phase ceramics;[18] (d) mechanics of biological materials for simulating brain tumor growth and its impact on surrounding tissues;[19] and (e) linear elasticity and thermal conductivity of two-phase polycrystalline ice cream[20] to design the structure needed for prescribed taste and texture. Shock-compression response of materials has been studied by Benson,[21] who utilized a pixel-by-pixel correlation technique to import the microstructure of HMX into Raven,[22] to simulate local temperature variations during shock-propagation in faceted and equiaxed HMX crystals. Benson[23] has also used real microstructures to accurately reproduce the equation of state of Cu. Use of real microstructures has also been made to describe the shock-compression response of reactive mixtures under uniaxial-strain[24,25] and uniaxial-stress[26] loading. These studies have demonstrated that real imported microstructures allow more accurate predictions in systems with inherent heterogeneities that significantly influence the phenomena or processes being investigated. Use of real microstructures also makes it possible to correlate mathematical representations of the microstructure for correlation with performance, thereby attaining the most robust predictive capability and enabling the reverse design of meso-scale structure for required performance characteristics, which will be the focus of the proposed work.

2.4   Microstructure Generation and Quantification

Meso-scale microstructures of multi-phase Ti+Al+B intermetallic-forming reactive materials are *three-dimensional* (3-D) and stochastic, with geometrical shapes that are complex, morphological orientations that are not necessarily isotropic, distributions of reactants that are not necessarily uniform-random, spatial correlations and clustering that exist frequently, and interactions/correlations among features occurring at different length scales. The geometric complexities present challenges for quantitative characterization, statistical representation, and simulations of microstructures, but also provide opportunities to optimize materials properties and enhance their performance. In this work, we have incorporated *real reconstructed* high-resolution large-volume 3D microstructures as RVEs to capture the complex meso-scale geometries of reactants. It build on our prior work on montage serial sectioning[27,28,29] and reconstructing images[30,31,32] for FE simulations,[33,34,35] to establish a framework for predicting the macro-scale performance of advanced reactive materials.

7

Statistical Representation of Microstructures: A microstructure is an ensemble of volumes, internal-surfaces, lines, and points. Depending on its dimensionality, each microstructural feature (particle, pore, grain) has an associated size, shape, volume, surface area, curvature, orientation, and location. Specification and statistical representation of the ensemble geometry requires quantification of volume fraction, total surface area, size distributions, etc., as well as descriptors of spatial arrangements, morphological anisotropy, and topology. Stereology techniques are well established for efficient/unbiased estimation of volume fraction, total surface area per unit volume, length per unit volume, number per unit volume, and integral mean curvature.[36,37] Statistical distribution functions such as *n-point* correlation functions and lineal path probability distributions go a step further and provide information on spatial arrangements (clustering, etc.) and anisotropy, for statistical representation of microstructure[38,39] and for use as robust descriptors for computer simulations of *realistic* microstructures. For a 3-D microstructure an n-point correlation function $P_{i, j, k, ...}(r_1, r_2, ...r_n)$ is the probability that a randomly located polyhedron having *n*-vertices, edge lengths r_1, r_2, ..., and specific orientation superimposed on a microstructure is such that its first vertex lies in the phase *i*, second vertex lies in the phase *j*, and so on.[40] Figure 2 illustrates examples showing (a) two-point, (b) three-point, and (c) four-point correlation functions in Al+SiC two-phase material. Another statistical descriptor is the lineal path probability distribution $L_{ii}(r, \theta, \varphi)$, which is the probability that a randomly located line in the microstructural domain of interest having length *r* and angular orientation (θ, φ) in the 3-D space is *completely contained* in the phase *i*. The variation of this probability with line length *r* and its angular orientation (θ, φ) contains microstructural information not available with correlation functions. In the proposed research, unbiased stereology and image analysis based computation techniques[42,43] will be used to obtain first-order global microstructural properties (volume fraction, surface area per unit volume, etc.), correlation functions, and lineal path probability distributions for detailed statistical representation of the microstructures, and to establish quantitative relations between
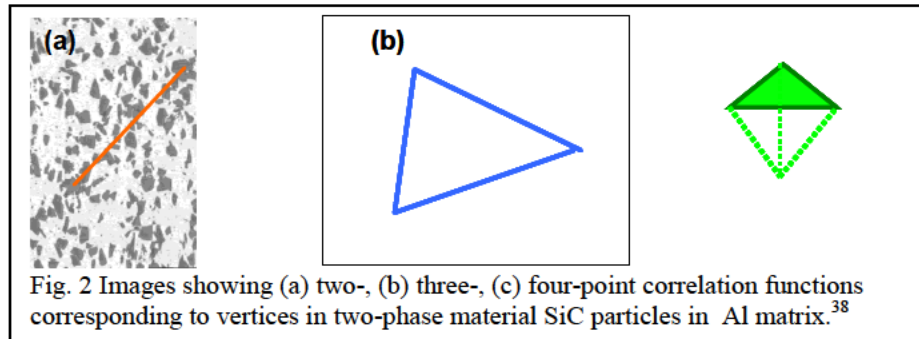

Fig. 2 Images showing (a) two-, (b) three-, (c) four-point correlation functions corresponding to vertices in two-phase material SiC particles in Al matrix.[38]

processing, structure, and properties.

Reconstruction of 3-D Microstructures: Random independent 2-D metallographic sections do not contain all information concerning the true 3-D microstructural geometry. Information regarding true 3-D particle/feature shapes/morphologies, spatial clustering and correlations, and topological aspects such as 3-D connectivity (e.g., of pores) does not reside in random independent 2-D metallographic sections.[40] Hence, incorporation of high-resolution large segments of realistic 3-D microstructural images as RVEs in computations, is *required* to account for effects of these important attributes on material behavior.[33] We have developed an efficient montage-based serial sectioning technique[41] for generation of large volume segments

of high resolution 3-D microstructures from stacks of aligned montage serial sections, and successfully applied to reconstruct 3-D microstructures of numerous materials,[25,33,34] which will be used in the proposed work. Figure 3 illustrates an example of 3-D microstructures reconstructed from montage serial sections. Complete reconstructed 3-D volumes are much larger than those depicted. High-resolution large volume segments of 3-D meso-scale microstructures of reactive materials will be constructed using this reconstruction methodology

Fig. 3. Reconstruction of 3D microstructure of Al-alloy composite containing SiC particles having 8.1 particle size ratio (PSR). (a) Stack of small number of digitally compressed aligned montage serial sections created by stitching 100 contiguous microstructural fields. (b). Each field of view in (a) was acquired at resolution depicted in (b); (c) Example of small segment of reconstructed 3-D microstructure depicting clustering of SiC particles.[41]

3.   TECHNICAL APPROACH AND SIGNIFICANT RESULTS

Advanced reactive materials based on the intermetallic-forming Ti+B+Al system were investigated in this work. The mixtures of the reactive elemental systems represent constituents that undergo highly exothermic anaerobic reactions, while also making it possible for residual reactants to become heated for subsequent (combustion) reactions. Various possible intermetallic and elemental combustion reactions can occur during impact loading of Ti+B+Al mixtures. The equilibrium heat of reaction[10] of combustion of Al (ΔH_R=-7422 cal/g), Ti(ΔH_R=-4714 cal/g), and B(ΔH_R=-14050 cal/g) is higher than that of intermetallic reactions, e.g., Al+2B (ΔH_R=-371 cal/g), 2Al+Ti(ΔH_R=-314 cal/g), and 2B+Ti(ΔH_R=-1320 cal/g). The threshold for reaction initiation is more dependent on the volumetric distribution of reactants, their intrinsic properties, and morphologies, rather than the heat of reaction. The constituents have varying intrinsic elastic/plastic properties, and the differences in these properties affect the extent of their deformation and fracture, the degree of their dispersion and mixing, and resulting threshold for reaction initiation. In the case of Ti+Al+B, the large difference in flow stress between Ti and Al ($\Delta \sigma_y$>100 MPa) can lead to extensive flow of Al without significant straining of Ti, which limits their mixing. However, the brittle behavior and high sound speed of B (ΔC_o~10km/s), in spite of its low strength, can force its dispersion and mixing with Ti.[42]

In addition to the constituent characteristics, the onset of reaction is also influenced by the state of loading involving uniaxial stress or uniaxial strain conditions. Hence, the overall

9

approach adopted in this work was to employ controlled gas gun experiments investigate (a) impact-initiated combustion reaction of aluminum powders of varying morphology under conditions of uniaxial-stress loading, (b) impact-initiated reactions in Ti+Al+B mixtures (Ti+2B mixed with varying contents of Al) under conditions of uniaxial stress loading, and (c) shock-compression of binary Ti+2B powder mixtures under conditions of uniaxial-strain loading. Meso-scale simulations with actual (real) and simulated microstructures were also performed with synthetic (simulated) microstructures generated from a library of constituent morphologies of particles and validation through two-point nearest neighbor correlations. The significant results obtained during the course of this work are detailed next.

3.1   Impact-initiated combustion of aluminum

The mechanisms of impact initiated combustion of aluminum powders of different sizes, morphologies, and pre-conditioning were investigated using uniaxial-stress rod-on-anvil impact loading with the 7.62-mm single-stage gas-gun. Aluminum powders of a range of particle sizes and exposed to mechanical pre-activation were studied to analyze the aluminum combustion reaction occurring during crush-up or subsequent compact deformation. The initiation mechanism, either thermochemical, due to densification and deformation of the compact, or mechanochemical, due to particle-particle interactions, or a combination of both mechanisms, were examined. A clear understanding of the mechanisms responsible for the combustion reaction in aluminum powder compacts can aid in the determination of the primary reaction process during the reactions of binary and ternary Ti+Al+B intermetallic-forming mixtures.

Reactivity of Aluminum Powders of Different Sizes and Size Distributions: The initiation of the aluminum combustion reaction under high-strain-rate impact-loading conditions was investigated by determining the onset of reaction as a function of aluminum particle size, particle size distribution, density of the compacts, and impact velocity. Spherical, as-received aluminum powders of four different diameters were investigated, a ~3μm diameter powder (Valimet H-2, Figure 4a), a ~9μm diameter powder (Valimet H-5, Figure 4b), a ~30μm aluminum powder (Valimet H-15, Figure 4c), and a ~75μm aluminum powder (Valimet H-60, Figure 4d). A Saltykov analysis of the particle size distribution gave a normal particle size distribution for the as-received powder sets. Additionally, mixtures with a bimodal size distribution were created by combining H-60 and H-2 powders in a 1:3 ratio (Figure 4e) and a 3:1 ratio (Figure 4f) and mixing in a V-blender.
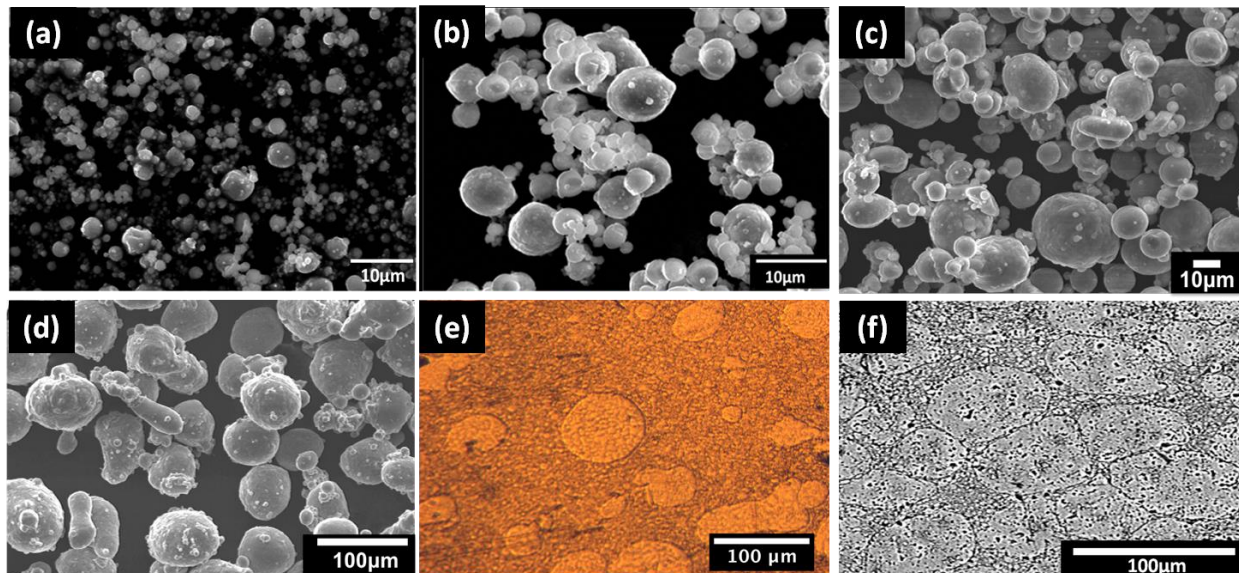
Figure 4. Images of aluminum powder mixtures tested. SEM images of Valimet H-2 (a), H-5 (b), H-15 (c), and H-60 (d). Light microscope images of bimodal mixtures of H-60 and H-2, 1:3 H-60:H-2 (e) and 3:1 H-60:H-2 (f).

SEM and XRD analysis were performed on both the as-received and highly-strained aluminum powders. XRD line-broadening analysis employing the Williamson-Hall method was used to determine the retained lattice strain in each type of impacted sample.

All starting powders were quasi-statically pressed into compacts of 2.0 ± 0.1mm height and 3.19mm diameter, ranging in density from 80% to 99% TMD. The surface area to volume ratio (S_v) of each powder type was measured by the intersection counting method from compacts of the pressed powders. The compacts were cross-sectioned, polished, etched, and imaged by light microscopy (Leica DM IRM). Cycloids were super-imposed on the image, and the average number of intersections between the cycloid and the microstructural boundaries per unit of the cycloid length (P_L) were related to the surface area per unit volume, S_v, via the relationship, $S_v=2P_L$.

The aluminum powder compacts were affixed to the lapped end of a copper projectile (38.1mm high x 7.62mm diameter) via 24 hour Hysol and impacted against a hardened steel anvil using the 7.62mm gas gun. The impact event was imaged via a high-speed framing camera (IMACON 200) in order to determine the initiation of combustion reaction during impact.

The observation of light in several consecutive frames captured by the high-speed framing camera was used as evidence of the occurrence of impact-induced combustion reaction, as shown by the example of images of a HEBM aluminum powder compact, illustrated in Figure 5. Each powder compact was tested at a range of velocities, from 140 m/s to 320 m/s, to determine the minimum velocity necessary for reaction to initiate under each condition. All experiments were performed under ambient environmental conditions.
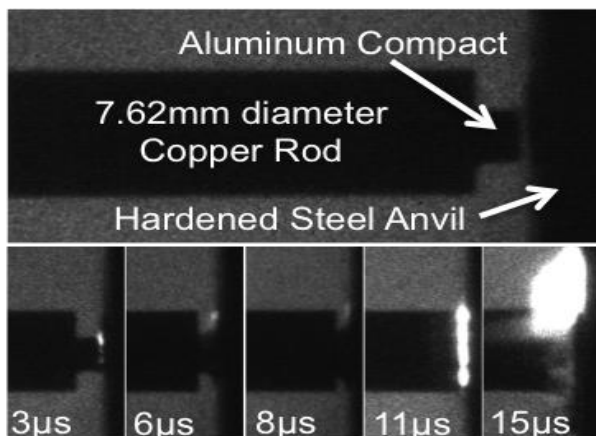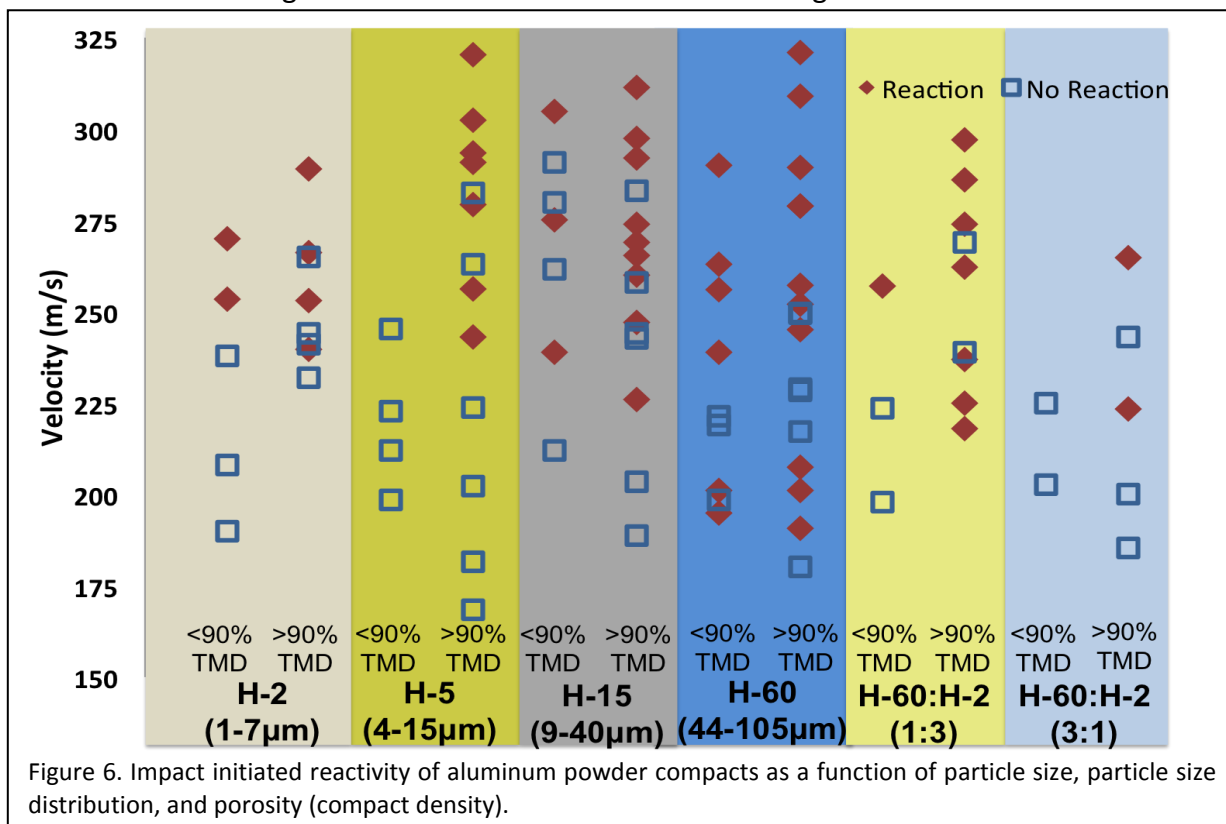
Figure 5. High-speed images of a HEBM aluminum powder compact affixed to a copper projectile impacting a hardened steel anvil at 302 m/s. Top image taken immediately prior to impact. Images after 3, 6, and 8 μs following impact show light emission during compaction and deformation of pellet, the image at 11 μs following impact show light emission after complete deformation of the compact, and the final image at 15μs after impact shows sustained reaction of the HEBM pellet as the Cu projectile also deforms upon making contact with the anvil.

The reactivity of each powder compact type was plotted against the measured impact velocity (Figure 6). Reaction occurrence was observed to vary as a function of particle size, with lowest velocities necessary for reaction initiation ranging from 190m/s to 240m/s. The smallest particle sizes, H-2 (~3µm) and H-5 (~9µm), showed the highest initiation threshold velocity (~240m/s), while the largest diameter particles, H-60 (~75µm), required the lowest velocity (~190m/s) to initiate reaction. In general, reactivity increased with particle size. The 1:3 and 3:1 bimodal mixtures both showed reaction at velocities (218m/s and 223m/s, respectively) between the largest and smallest particle sizes. Additionally, the general reactivity trends for each powder type indicate that porosity (or compact density) also plays a role in the initiation of the combustion reaction in the Al powder compacts. Compacts with densities between 80 and 90% reacted at higher velocities than those with densities greater than 90% TMD.

Figure 6. Impact initiated reactivity of aluminum powder compacts as a function of particle size, particle size distribution, and porosity (compact density).

12

Reactivity of Aluminum exposed to mechanical pre-activation: The effect of mechanical pre-activation on the impact-initiated combustion of aluminum powder compacts was studied by comparing the impact response of as-received aluminum powders to those strain-hardened by either ball-milling or by high-strain machining. High energy ball milled (HEBM) powders were prepared by loading 5 g of Valimet H-60 aluminum powder into an alumina vial and ball milling with five alumina spheres of 6.3mm diameter, using a SPEX mill for 10 minutes, 30 minutes, and 60 minutes (Figure 7a-c). During the milling process, the spherical powders were observed to fracture, plastically deform, and cold weld. As the ball milling time increased, the particles became more flattened, flake-like, and gave a bimodal particle-size distribution centered around 70 to 800µm diameter. The second mechanically pre-activated powder type, highly strained aluminum 6061 chips (figure 7d), was prepared by Shankar et. al.[43] using a plane-strain machining method. These chips contain ultrafine grains that strengthen the Al6061 and are approximately 80µm x 80µm x 30µm in size.[44]
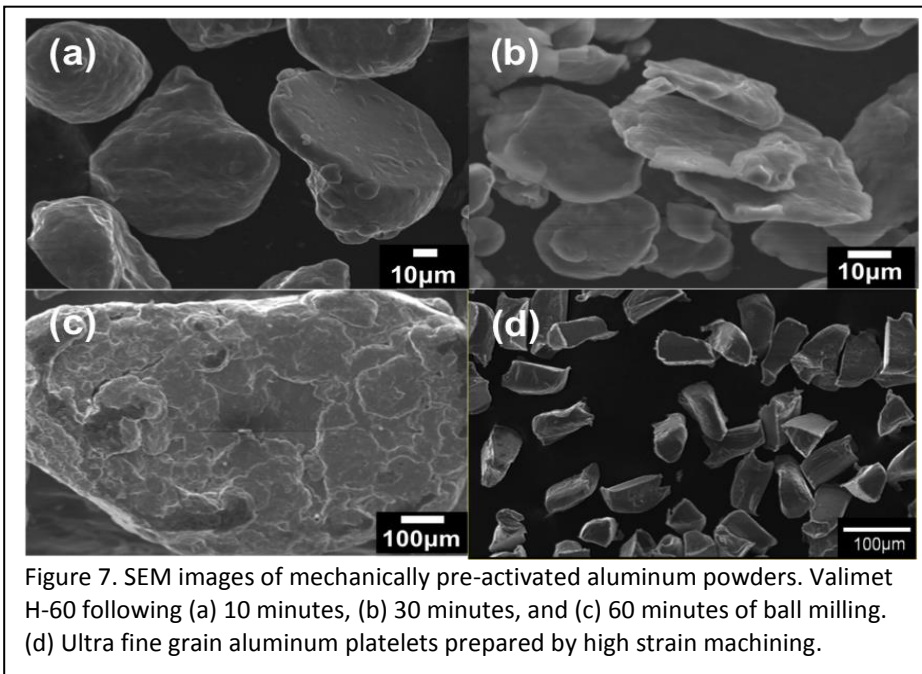

Figure 7. SEM images of mechanically pre-activated aluminum powders. Valimet H-60 following (a) 10 minutes, (b) 30 minutes, and (c) 60 minutes of ball milling. (d) Ultra fine grain aluminum platelets prepared by high strain machining.

The impact-initiated reactivity of each powder compact type, obtained from rod-on-anvil impact experiments described above, is plotted as a function of the measured impact velocity, as shown in Figure 8. It can be seen that after processing via high energy ball milling for 10 minutes, the reactivity of H-60 aluminum decreases, requiring impact velocities of at least 215m/s to react. Yet, as ball milling times are increased to 30 minutes, the reactivity improves, with reactions observed at velocities as low as 175m/s. Compacts of Valimet H-60 samples ball-milled for 60 minutes, highly-strained aluminum platelets, and mixtures of H-60 and platelet powders, are observed to be less reactive than H-60 powders, with reaction velocity thresholds in the range of 207 to 213m/s.

Figure 8. Impact initiated reactivity of aluminum as a function of mechanical pre-activation and porous density.
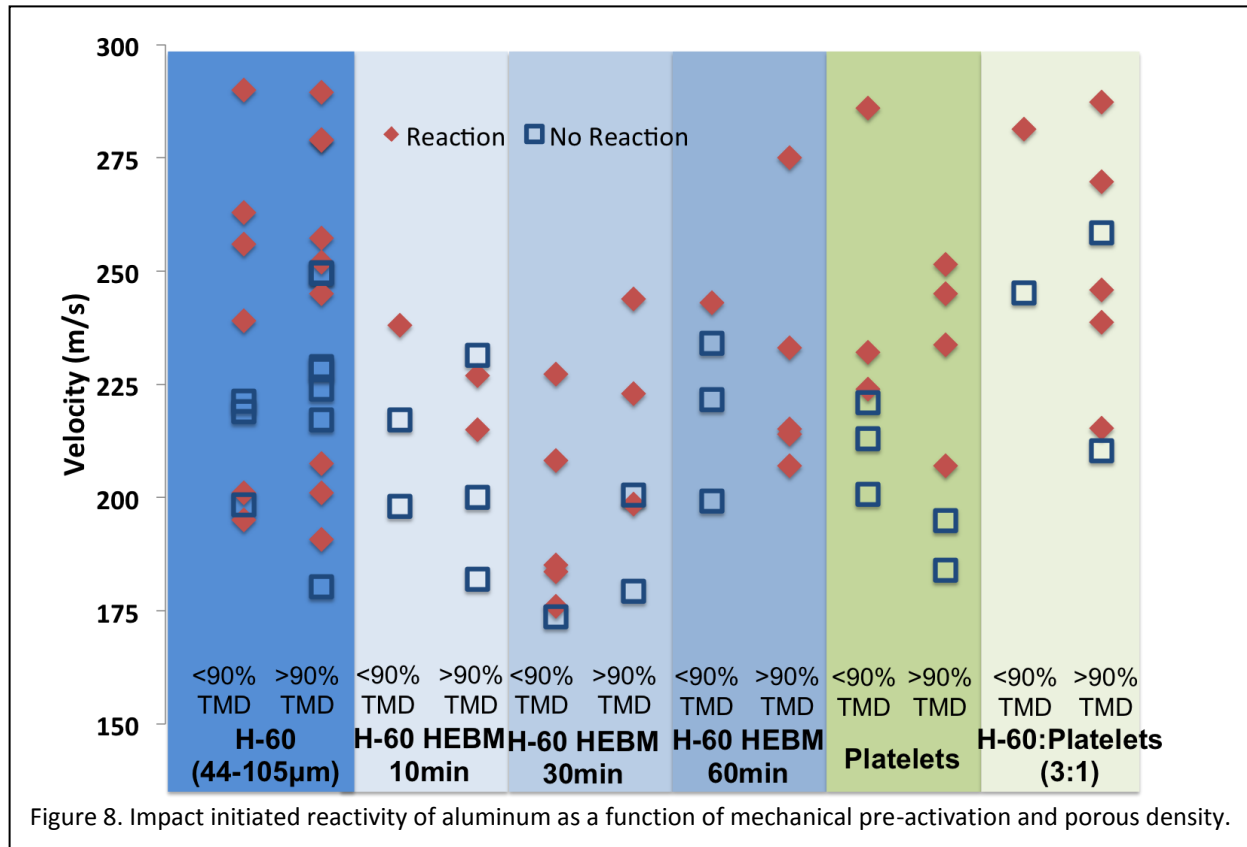
Possible mechanisms of impact-initiated combustion of aluminum powder compacts: The minimum (threshold) impact velocity for reaction initiation in compacts of aluminum powders is found to correlate with particle size, mechanical activation, and compact density based on the results depicted in Table I. Mechanical pre-activation of the aluminum powders both strain hardens the material and exposes fresh reactant surfaces. Strain hardening was confirmed from retained elastic strain measured using the Williamson-Hall XRD peak broadening method.

Table I. Summary of aluminum powder properties

Particle Type	~Particle Diameter Range(μm)	Surface Area per unit Volume (mm^{-1})	Lattice Strain	Vickers Hardness Value	Threshold Velocity (m/s)
H-2	1-7	1885.7	-	-	240
H-5	4-15	824.3	-	-	240
H-15	9-40	441.9	-	-	226
H-60	44-105	105.7	-		190
H-60 HEBM 10min	44-250	108.3	.0013		215
H-60 HEBM 30min	44-500	166.9	.0006		175
H-60 HEBM 60min	60-750	237.5	.0005		207
Platelets	80	196.2	.0049		207

The lattice strain for highly-strained aluminum 6061 platelets was significantly greater than the lattice strain of any other sample tested, but it resulted in decreased reactivity, in terms of a higher threshold velocity. On the other hand, Valimet H-60 powders exposed to mechanical pre-activation via HEBM, showed enhanced reactivity with lower threshold velocity. Strain hardening by mechanical pre-activation can have a pronounced effect on particle-particle interactions, which influences the energy input necessary for compaction and deformation of the powder compact during impact. Reactivity of the highly strained aluminum 6061 powder compact was most likely decreased because the harder, stronger particles required more energy to be expended during compaction and deformation of the higher strength particles, leaving less energy available for reaction initiation. For the HEBM H-60 particles, high energy ball milling for a short period of time causes some strain hardening as observed by the measured lattice strain but also breaks the particles into smaller sizes (up to 30 minutes milling) before re-welding and agglomerating the powders with further milling time. The 3-minute HEBM samples appear to exhibit the best case scenario for mechanical pre-activation resulting in creation of fresh reactant surfaces due to break-up of particles, which leaves a thinner, more easily penetrable Al_2O_3 coating, thereby enhancing the reactivity during subsequent impact.

With respect to particle size, the threshold velocity for reaction of compacts of aluminum powders is observed to decrease with increasing particle size. The 1:3 bimodal particle size distribution shows decreased reactivity (higher threshold velocity). Both smaller particles and the bimodal particle size distribution result in a powder compact that is denser with smaller more uniform pore spacing, than a compact composed of mostly larger particles. Compacts containing larger particles have larger, more randomly distributed pores and are therefore subjected to increased plastic deformation and heating during the compaction and deformation process during impact. Although more energy is necessary to plastically deform the particles, the enhanced heating serves to augment the reaction in the larger particles.

The validity of these possible mechanisms for impact initiation of combustion reactions in the various aluminum powder compacts can be further verified by employing a transparent sapphire anvil (Figure 9), instead of the high strength steel anvil. Use of a transparent sapphire anvil allows observation of reaction at the impact face, thereby enabling evidence of reaction initiation associated with compaction or compact deformation processes during impact.

Figure 9. Schematic of sapphire anvil set-up (a) and Imacon high speed images of reaction occurring at the impact face of the sapphire anvil.
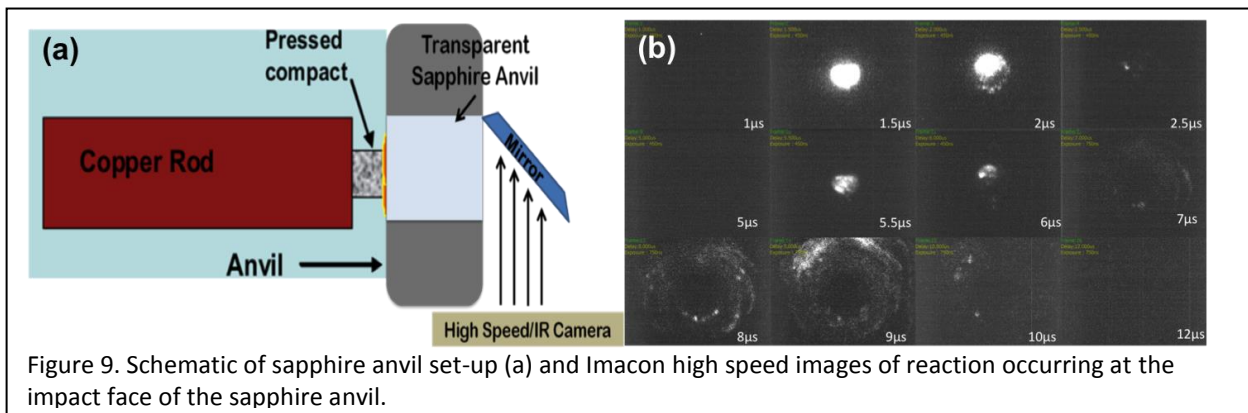
Figure 9 shows a schematic of the sapphire anvil setup and images of an aluminum powder compact impacting the sapphire anvil. A frame is captured every 500ns and the images show an initial impact flash that is extinguished within 1µs, followed by reaction light that observed in a few localized areas within the compact. These images need to be correlated with a profile view of the impact process to determine at the stage of impact at which the reaction occurs during powder densification, compact deformation, or post-deformation as the copper projectile interacts with the anvil. Additionally, IR imaging can be employed in conjunction with the sapphire anvil (as shown in Figure 10) in order to identify the nature of heating occurring during reaction, whether localized or bulk. The analysis of impact initiation trends as a function of particle size, porous density, and mechanical pre-activation can then be correlated with *in situ* time-resolved analytical methods, including IR camera measurements and UV/Vis spectroscopy, to identify the source of the differences in reaction phenomena between compacts of aluminum powders of different characteristics.
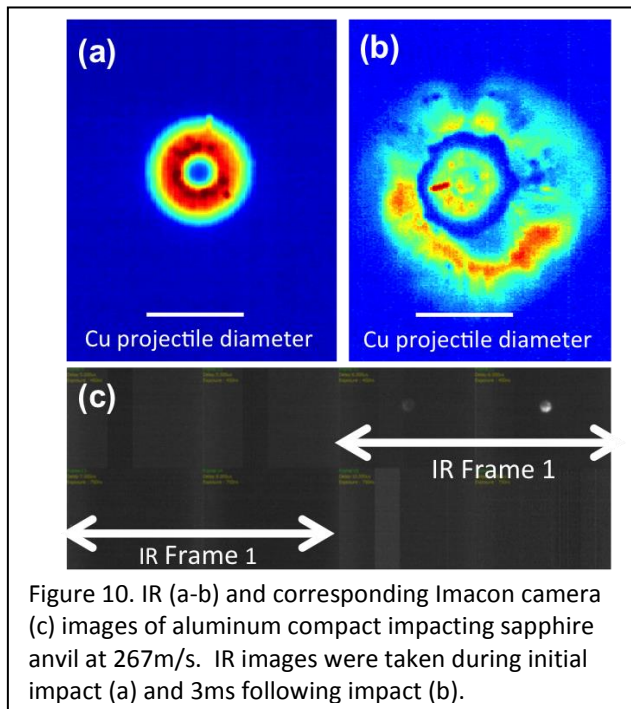

Figure 10. IR (a-b) and corresponding Imacon camera (c) images of aluminum compact impacting sapphire anvil at 267m/s. IR images were taken during initial impact (a) and 3ms following impact (b).

3.2 Impact-initiated Reactions in Ti+Al+B Mixtures Under Uniaxial Stress Loading

The objectives of this task are to investigate the reaction behavior of mixtures in the Ti+Al+B system with Ti+2B mixed with varying volume fractions of Al powders. Ultimately, we seek to understand the reaction mechanisms in this ternary system and to explore the synergistic effects that Ti+B intermetallic reaction may have on Al powders in promoting an oxidation reaction. Moreover, this work aims to quantify the extent of the role that meso-scale features (extrinsic properties) play in ensuring the right thermodynamic conditions are ensured so that these systems may react in a deterministic manner. The investigation involved performing experiments under uniaxial-stress and simulating experimental conditions using realistic microstructural representations using CTH hydrocode.

Uniaxial stress rod-on-anvil impact experiments were performed on Ti+Al+B mixtures, varying in composition from 0% Al to 75% Al by volume and mixed with stoichiometric Ti+2B. The powder mixtures were pressed into 1/8" diameter pellets and mounted on copper rods which were impacted against a steel anvil in the 7.62 mm gas gun. A number of impact experiments characterized using high speed video and a framing camera were conducted to observe the reaction event confirmed via light emission. The "go/no-go" experiments revealed whether the pressed powder mixture pellet produced light emission (indicative of reaction as

16

shown in representative micrograph in Figure 11) at a certain firing velocity (kinetic energy), which was used to determine the "threshold" energy for reaction initiation.

75% Al – 25% Ti+2B
Velocity = 454.21 m/s

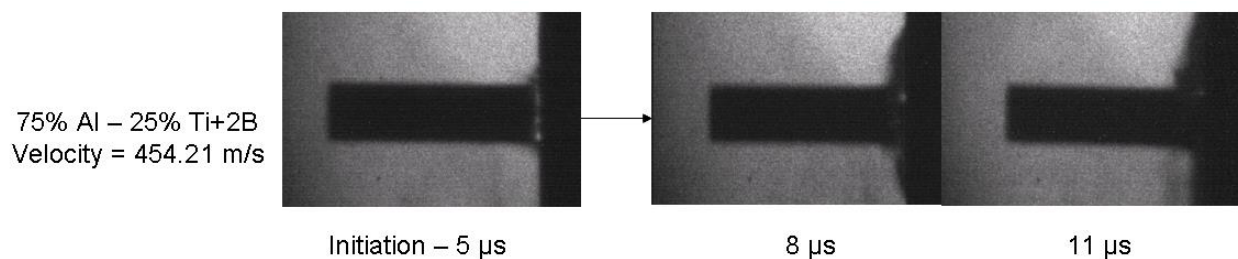Initiation – 5 µs   8 µs   11 µs

Figure 11: Representative images of typical light emission observed in a rod-on-anvil impact experiment, indicative of possible initiation of intermetallic or oxidation reaction.

It was found that the 50%Al mixture reacted most easily under uniaxial stress conditions, as evidenced by its lower reaction threshold energy versus that for the more deficient (pure Ti+2B) and Al-rich Ti+2B + 50 vol% Al mixtures. The enhanced reactivity of this mixture can be related to the competition between dissipative mechanisms being prevalent in Al deficient mixtures and localization being hindered with higher Al content mixtures. Results of the go/no-go reaction experiments are summarized in Figure 12, which plots impact energy against material composition with pure Al composition (over 90% TMD) added for comparison.

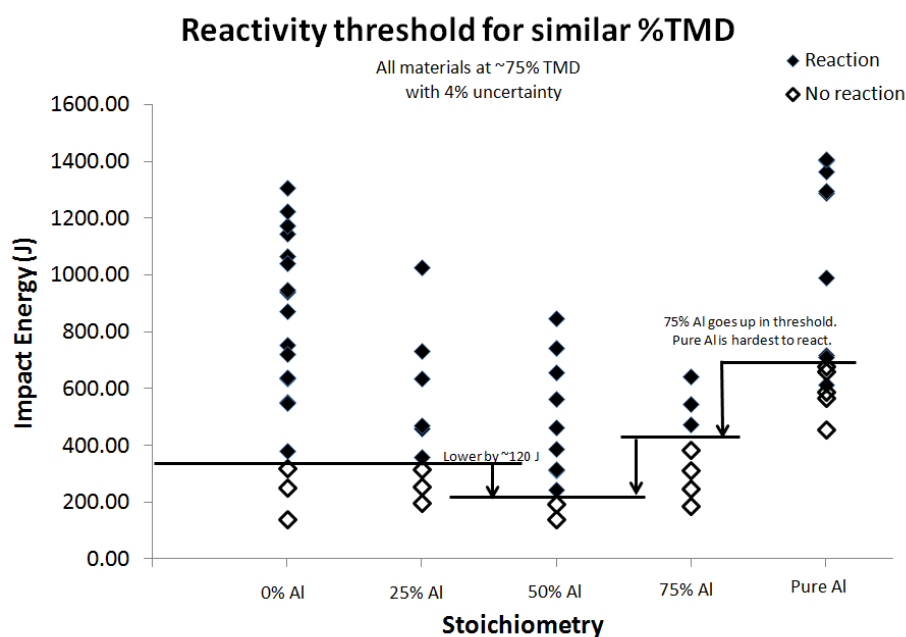Figure 12: Reaction threshold map showing the energy requirements to observe reactivity under uniaxial stress conditions for a variety of stoichiometries.

A lower reaction threshold, defined as the amount of energy required to observe light emission in more than two frames during impact, is observed for the 50% Al stoichiometry than for any of the other mixtures. Aluminum deficient materials show a slightly higher reaction

17

threshold. The reactions observed in Al deficient materials are likely driven by frictional heating and localized hot-spot formation as a result of pore collapse during the compression process. The Al rich mixtures rely on strain localization phenomena to initiate a reaction. However, for greater Al content, the amount of Ti+2B to satisfy stoichiometric requirements in the mixture needs to decrease. This may lead to any reaction initiation being quenched before a sustained reaction between the Ti+2B can sufficiently ignite the Al reaction. The lower temperatures in Al-containing materials may be sufficient to enhance diffusion-controlled reactions in Al, which can trigger the Ti+2B reactions. Quantitative stereology has revealed that a more intimate contact between Ti and B can be obtained during mixing in the presence of Al content. The mechanistic effects at the meso-scale, that affect the reaction initiation behavior of these materials was further investigated using numerical simulations.

Uniaxial stress simulations were performed on the Ti+2B+Al powder mixtures using real microstructures. Figure 13 shows the simulation domain with explicit description of boundary conditions. Results of simulations performed at 200 m/s reveal substantial agglomeration of smaller boron particles in well-defined dark bands near localization regions of large Ti or Al deformations, as shown in Figure 14. Large temperatures, in excess of 1200° C are observed even at low impact velocities in Ti+2B mixture (with 0% Al), largely due to the large pore space where particles can mix and deform. This leads to increased friction and deformation of softer load-carrying Al and Ti particles which account

Figure 13. Uniaxial stress simulation domain with explicit description of boundary conditions.

for the high temperatures. While local temperatures are higher in Ti+2B, bulk temperature remains low which can account for higher reaction threshold. Bulk temperatures in Al-containing structures are sufficient to cause Al to melt and thus possibly lead to a potential liquid-phase mediated reaction mechanism. Transport phenomena are currently being studied using stereological metrics to assess the evolution of particle interfaces, agglomeration, and hot spot regions. The agglomerated structure is better visualized in the zoomed-in view with the superimposed temperature field, as shown in Figure 15. Both, the 0% Al and 50% Al structures show pronounced banding and agglomeration. However, the number of small boron agglomerates is much higher for the 0% Al structure, indicating that the presence of Al somewhat reduces the boron agglomeration. This may be due
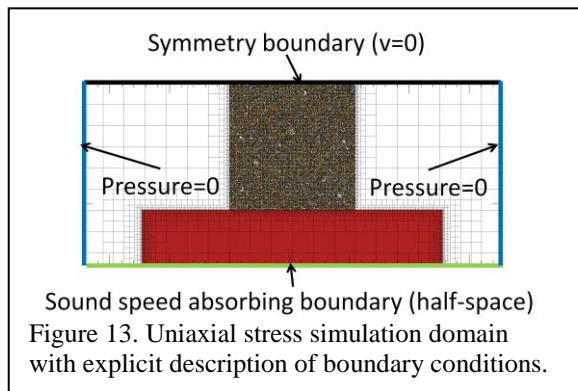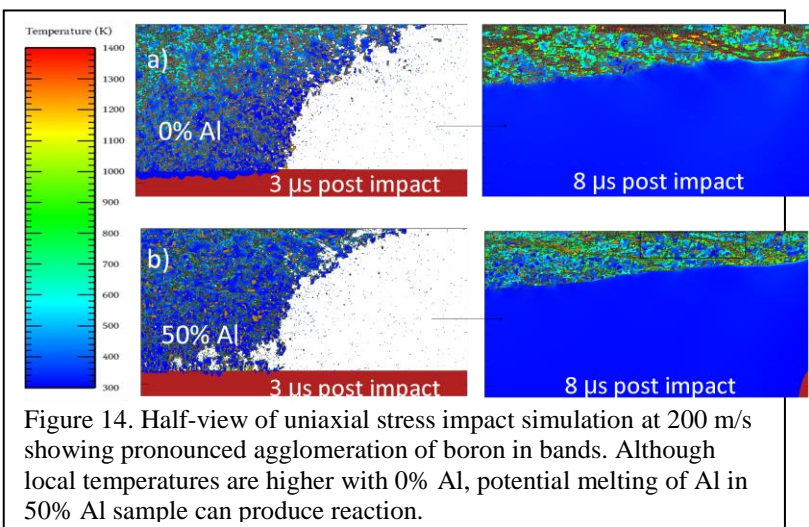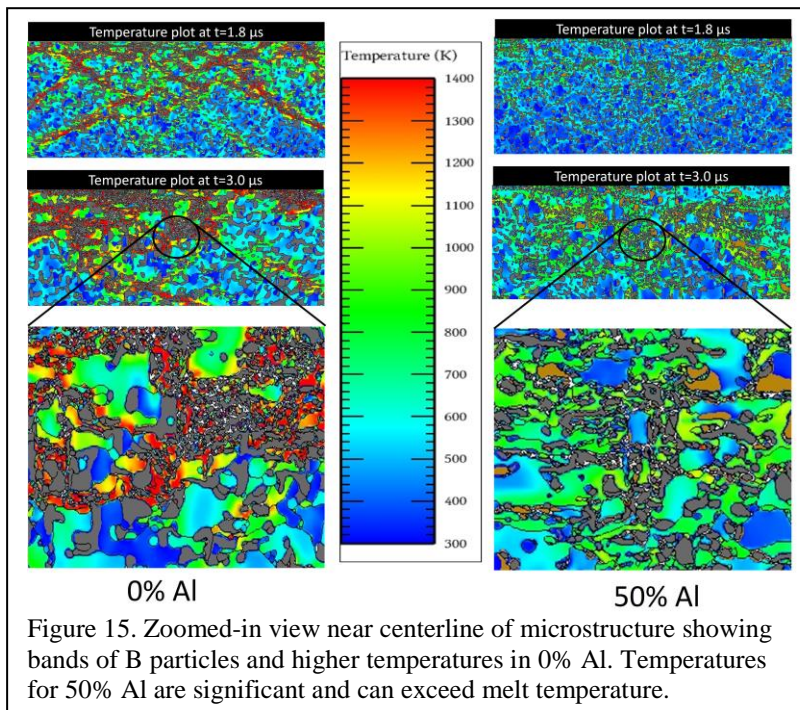

Figure 14. Half-view of uniaxial stress impact simulation at 200 m/s showing pronounced agglomeration of boron in bands. Although local temperatures are higher with 0% Al, potential melting of Al in 50% Al sample can produce reaction.

to Al preferentially shearing and filling empty space, whereas the 0% Al structure depends on shearing of Ti and movement of the smaller B particles to fill the empty spaces during crush-up.

The zoomed view in figure 15 compares regions near the middle of the structure for different times. The structure of the agglomerates is revealed as colonies of boron particles, stretched and in some cases pulverized (most prevalent in the 0% Al structure). The boron particles are much more equiaxed in the 0% Al structure than in the 50% structure. The Al in the 50% structure carries boron along as it deforms, whereas the 0% structure leaves greater open spaces since the Ti does not deform as readily. These open spaces do not permit boron deformation. Instead, boron agglomerates

Figure 15. Zoomed-in view near centerline of microstructure showing bands of B particles and higher temperatures in 0% Al. Temperatures for 50% Al are significant and can exceed melt temperature.

and fractures during the mixing phase within these open spaces (i.e. pores). The bulk temperature also is much greater in the 0% Al structure where the heating is based on the plastic dissipation in the Ti and the interparticle friction between Ti and B surfaces. These dissimilar effects, most clearly demonstrated by meso-scale simulations illustrate the effects of the reactant configuration on impact-initiation of reactions in Ti+Al+B ternary mixtures.

3.3   Shock-compression of Ti+2B powder mixtures: Experiments and Simulations

The highly heterogeneous starting Ti+2B powder mixtures and the continually evolving nature of the heterogeneities can result in various reaction pathways which make tailoring of the reaction configuration a challenge to design. The Ti/B system is of particular interest because of the extraordinarily high enthalpy of reaction (ΔH_{rxn}^0 = -320 kJ/mol) when forming the stable TiB_2 product phase. This unconventional energetic mixture has many key ingredients that can enable shock-induced reactivity due to meso-scale transport processes and strain localization phenomena enhanced by the very heterogeneous nature of these mixtures.[4,10]

Experiments: The shock compression response of 1:2 molar mixtures of Ti+B was investigated at shock pressures up to 5 GPa to probe the shock adiabat of this mixture for a 50% starting density. The shock compression regime was probed from crush-up to full density and onward to assess the potential onset of a shock-induced chemical reaction event in the powder mixture. PVDF stress gauges measure the shock speed and equilibrated stress at the gauge/powder

interface and the Velocity Interferometer System for Any Reflector (VISAR) was employed to compare the interface velocity at the powder/backer interface with the PVDF stress signal. A series of two-dimensional continuum meso-scale simulations on validated simulated microstructures were performed to predict the shock compression response and identify the meso-scale mechanics that are essential for reaction. The suitability of the simulated microstructural representations was evaluated by comparing the experimental and predicted pressure traces. The measured stress profiles are compared with meso-scale simulations of a highly resolved uniform-random mixture of Ti+2B also at 50% TMD. The measured backer stress gauge traces show an interesting "two-wave" rise-time structure stemming from particle avalanching effect caused by initial compression of loosely-bound particles near the surface of the PVDF stress gauge, followed by an avalanche of fully compressed particles increasing the stress to maximum levels. The simulations are found to generally over-predict the measured stress at the backer, though they capture the salient features of the rise-time effects caused by the heterogeneous powder compaction which manifest themselves in the averaged stress traces as discrete humps and compare very favorably with measured PVDF traces.

Uniaxial strain experiments were performed on mixtures of titanium (Atlantic Equipment Engineers ~625 mesh sponge) and boron (Alfa-Aesar Amorphous 94-96%, Mg nominal 1% < 5 micron irregular/flake) powders first dried at 110°C and then pre-mixed in 1:2 molar ratio in an inert atmosphere. The powders were sealed and transferred to a v-blender for further mixing (24 h) to ensure a uniform-random mixing of Ti and B. Further details of the powders used in this study can be found elsewhere.[45] Instrumented parallel-plate impact experiments on Ti+2B powders were conducted using the 80 mm helium-driven gas gun. A set of copper capsule fixtures were prepared to contain the powder mixture during the experiments. The capsules (Figure 16) consisted of an outer copper containment ring, copper driver plate, and transparent fused silica backer plate sandwiching the powder which was pressed onto a dummy driver at 50% TMD. The dummy driver was replaced with one containing the gauge package. Aluminum sabots carried the flyer plate (e.g., copper, tungsten, or tungsten heavy alloy depending on the desired impact stress) and impact
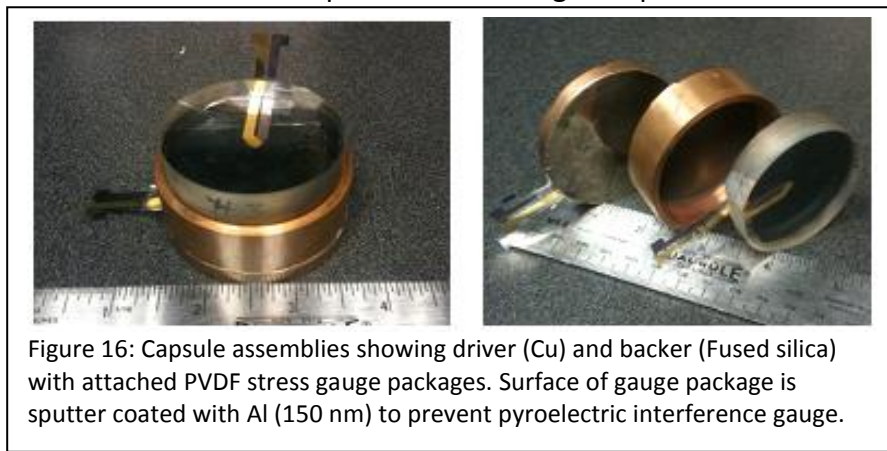
Figure 16: Capsule assemblies showing driver (Cu) and backer (Fused silica) with attached PVDF stress gauge packages. Surface of gauge package is sputter coated with Al (150 nm) to prevent pyroelectric interference gauge.

velocity was monitored by sequential shorting pins as shown in the schematic in Figure 17. PVDF stress gauge packages were mounted onto the driver and backer plates to monitor the stress state and wave arrival times at the front and back of the powder bed. The gauge packages consisted of alternating polytetrafluoroethylene (PTFE) layers to isolate the PVDF gauge, and a sputtered layer of Al (150 nm thick) at the end to mitigate the effects of pyroelectric interference on the PVDF gauge (Figure 16).

Figure17. Schematic of uniaxial strain impact experiment set-up. An Al sabot carries a copper impactor plate which impacts a Cu driver plate and imparts the shock into the powder backed by a fused silica backer plate. PVDF stress gauge packages sandwich the powder and provide stress and shock speed measurements.
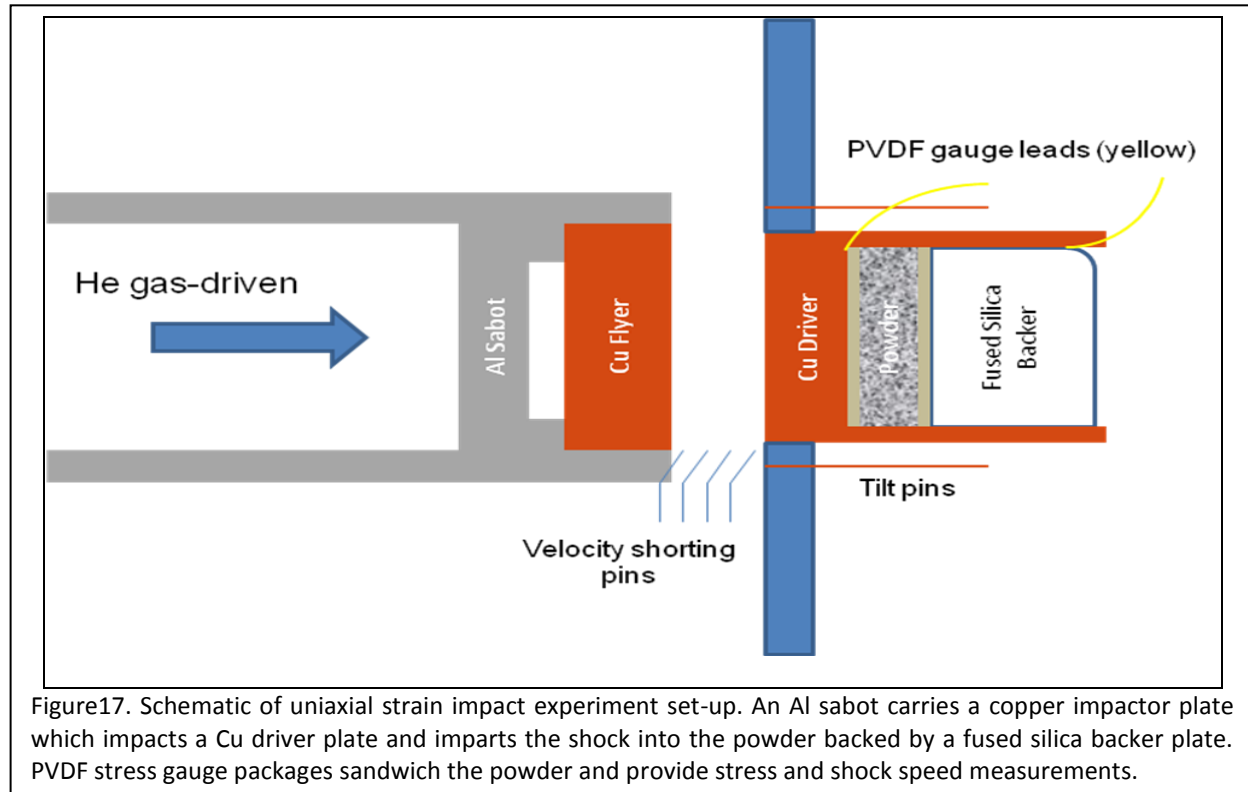
Figure 18 shows an example of stress profiles captured by the input and propagated PVDF stress gauge profiles. The PVDF gauges at the driver/powder interface showed anomalous signals at the peak stress in several experiments possibly due to gauge failure. Therefore, the shock input stress in the powder mixture was impedance-matched with the shock speed and impact velocity at the driver. The propagated gauge stress profiles captured at the powder-backer interface, reveal characteristic effects of wave dispersion associated with the heterogeneous nature of powder compaction. The effects are clearly revealed by the backer (propagated) stress gauge profiles shown in Figure 19. The transparent fused silica backer also permitted for simultaneous VISAR measurements through adequate preparation of the fused silica surface prior to attaching the gauge package. All mating surfaces were lapped to optical flatness (< 1 mrad tilt).

Figure 18. Typical stress profiles captured by input and propagated PVDF stress gauges.
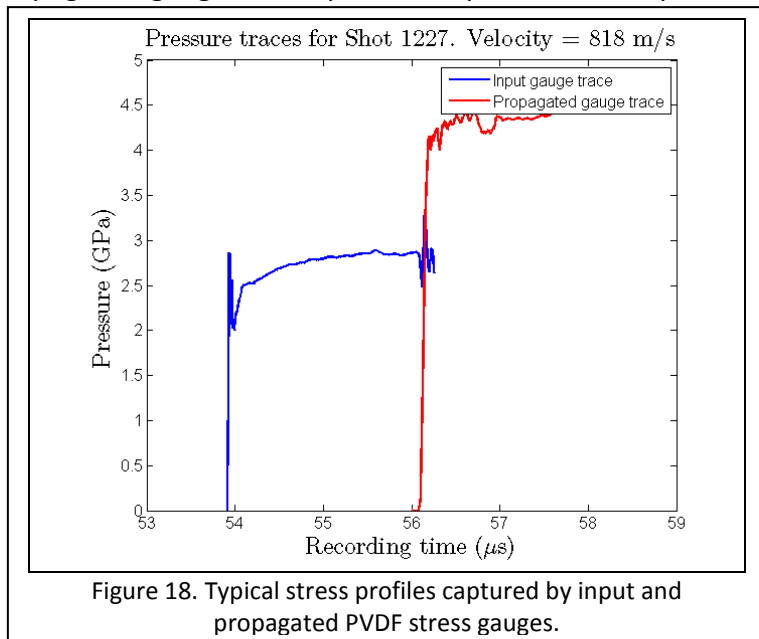
Uniaxial-strain plate-impact experiments provide the shock speed and equilibrated stress at the powder/backer interface. The results for each experiment are summarized in Table 2. The shock speed through the powder was calculated based on the transit time measured at the 10%, 50%, and 90% levels of the rise time to peak stress. This provides three independent measurements of shock

Figure 19. Backer stress traces show a variety of rise-time behaviors characteristic of highly heterogeneous mixtures. Trace for 818 m/s shows numerous signals which may be due to separate compression phenomena corresponding to two separate voltage spikes in raw signals (not shown). The higher imapct velocity and higher impedance flyer experiments show this same phenomean, but not as pronounced due to lower inherent dispersion in rise

speed, though one can see considerable scatter due to the dispersion at the backer gauge. The dispersion decreases as the impact speed and impactor plate impedance increase. The stress waves propagating through the powder mixture, and recorded at the interface with the backer plate, result in significant dispersion at lower impact velocities, which increases the transit time difference between rise time levels leading to increased uncertainty in the single shock speed value. The thickness of the powder was measured through five independent measurements with an accuracy of 0.005 mm. The greatest contribution to the uncertainty in thickness arises from irregularities during the initial pressing of the powders in the capsule. The overall results reveal no clear trend and no discernable evidence of a chemical event.

Table 2: Summary of experimentally-measured quantities and impedance-matched particle velocity and stresses for the shock compression experiments on Ti+2B.

Shot #	Flyer	V_{imp} (mm/µs)	U_s (mm/µs)	U_p (mm/µs)	σ_I (GPa)	V/V$_{00}$
1225	Cu	$0.513 \pm 0.35\%$	$1.23 \pm 4.14\%$	$0.48 \pm 7.08\%$	$1.06 \pm 4.06\%$	0.61
1227	Cu	$0.818 \pm 1.61\%$	$1.76 \pm 1.95\%$	$0.753 \pm 4.54\%$	$2.24 \pm 1.69\%$	0.57
1302	Cu	$1.044 \pm 3.66\%$	$2.16 \pm 5.30\%$	$0.944 \pm 3.62\%$	$3.63 \pm 1.49\%$	0.56
1307	Cu	$0.832 \pm 0.28\%$	$1.72 \pm 2.02\%$	$0.769 \pm 4.45\%$	$2.36 \pm 2.37\%$	0.55
1309	WHA	$0.921 \pm 0.52\%$	$1.79 \pm 3.68\%$	$1.01 \pm 3.38\%$	$3.83 \pm 15.7\%$	0.43
1310	W	$0.933 \pm 0.52\%$	$2.13 \pm 3.44\%$	$1.12 \pm 3.06\%$	$4.1 \pm 7.32\%$	0.48
1314	W	$0.890 \pm 0.66\%$	$1.81 \pm 0.40\%$	$1.08 \pm 3.17\%$	$3.84 \pm 13.01\%$	0.42
1320	Cu	$1.06 \pm 0.83\%$	$1.86 \pm 1.86\%$	$0.966 \pm 3.54\%$	$3.03 \pm 0.71\%$	0.48

Simulations: Realistic simulated microstructures were generated by inserting Ti particles from a specially-crafted library created through montage serial sectioning, and simulating boron particles through a polar plot of a Fourier Sine series. Further details of the method are described in a prior work.[30] The particles were inserted into a simulation domain one at a time with a strict overlap control. The size distribution for each component replicated the vendor-supplied information and a uniform-random distribution of constituents was generated. A 50% TMD uniform-random distribution of particles was achieved and validated through two-point correlation functions when compared with real microstructures.

Uniaxial-strain impact simulations were performed using the Eulerian hydrocode CTH (Version 9.0, Sandia National Laboratories 2009) by placing the microstructure in a 2D simulation domain with simulated PVDF gauge packages, Cu driver, impactor (either Cu or W), and fused silica backer as shown in Figure 20. The simulation set-up is a
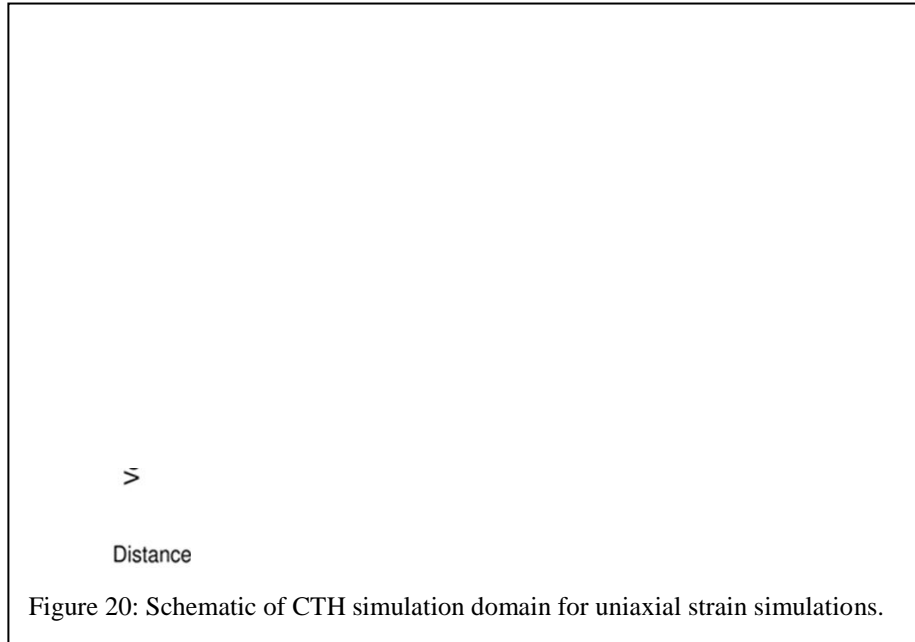
Figure 20: Schematic of CTH simulation domain for uniaxial strain simulations.

1:4 scale model of the experimental fixture. The left and right boundaries were set as periodic symmetry boundaries and the top and bottom boundaries were set as sound speed absorbing (half-space). The Ti particles were modeled with the rate-independent Steinberg-Guinan-Lund constitutive model. The Cu plates were modeled with the Zerilli-Armstrong constitutive model and the gauge package was made hydrodynamic. The fused silica backer employed a Johnson-Cook model and the boron particles used a Von-Mises yield surface with thermal softening. All constituents except for boron were modeled with the SESAME equation of state as provided by the built-in SESAME tables; Boron was

Figure 21. Temperature field for a 1000 m/s Cu/Cu impact on a 50% TMD Ti+2B powder.

modeled with a Mie-Grüneisen equation of state. A set of ten tracer points were placed at each PVDF gauge center to track the velocity, stress, and temperature. A typical temperature profile is shown in Figure 21 for a fully compacted structure.

The meso-scale microstructure-based simulations show a random distribution of hot spots exceeding 1400 K, but do not predict a large heat buildup in the bulk of the material. This can lead to quenching of any potential reaction. Temperatures remain nominally within the 700-1000K range, well below even the temperatures needed for thermally-induced reactivity in Ti+2B. Also, the diffusional processes within these temperature ranges are too sluggish to promote enhanced reactivity. However, there was some indication of shear banding caused by excessive deformation in the Ti particles, potentially l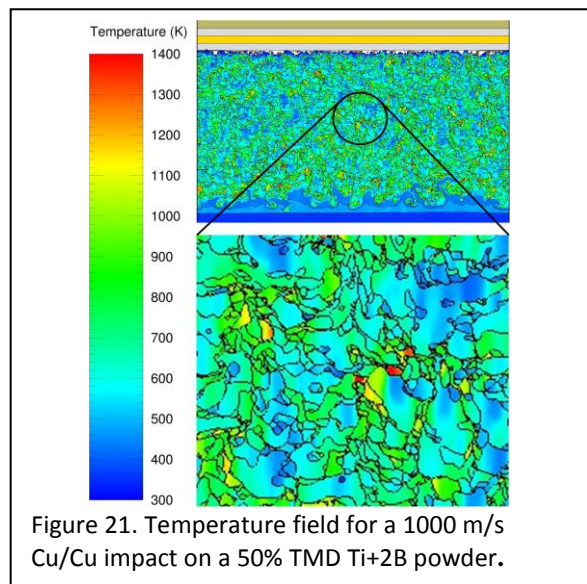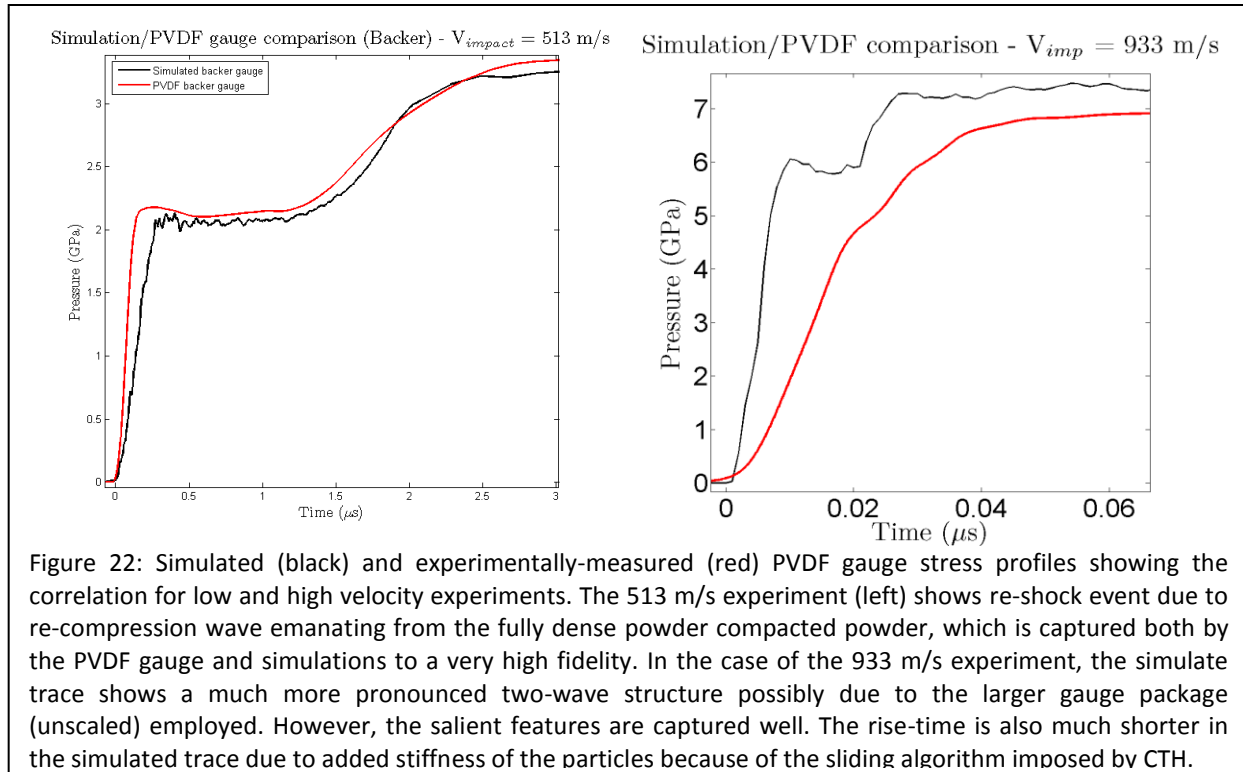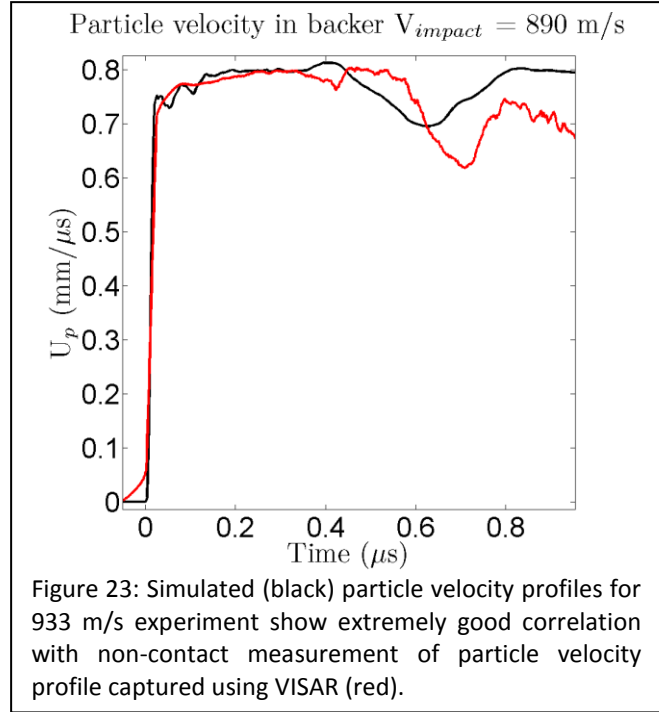eading to increased temperatures within the surrounding regions. The size disparity and differences in elastic-plastic properties between Ti and B particles, causes the B particles to agglomerate and confine between the larger Ti particles. However, the high strength of B and the geometry of the Ti particles do not permit large hydrodynamic transport as previously observed. This can unequivocally be shown through the evolution of surface area or B/B, Ti/Ti contact area as a function of simulation time. Studies are currently being conducted by varying extrinsic properties such as particle anisotropy, degree of starting agglomeration, and size distribution using a 2^k design of experiments framework to ascertain the sensitivity of the system to variations in adjustable parameters.

The recorded backer-gauge stress traces (Figure 22) show a dispersed ``two-wave'' structure, potentially due to differences in arrival times of the more loosely-bound particles near the surface of the PVDF gauge and the succeeding particle ``avalanche.'' The avalanching particles move at a group velocity impedance-matched with the Cu driver and slower than the initial jagged front. This initial front creates an initial shock compression of the gauge which rings up to peak pressure for about 10-20 ns, subsequently equilibrating with the more sluggish particles that follow. This is confirmed by simulations which reproduce the same behaviors (c.f. Figures 22) due to the continual compression of the backer by a fully compacted powder.

Figure 22: Simulated (black) and experimentally-measured (red) PVDF gauge stress profiles showing the correlation for low and high velocity experiments. The 513 m/s experiment (left) shows re-shock event due to re-compression wave emanating from the fully dense powder compacted powder, which is captured both by the PVDF gauge and simulations to a very high fidelity. In the case of the 933 m/s experiment, the simulate trace shows a much more pronounced two-wave structure possibly due to the larger gauge package (unscaled) employed. However, the salient features are captured well. The rise-time is also much shorter in the simulated trace due to added stiffness of the particles because of the sliding algorithm imposed by CTH.
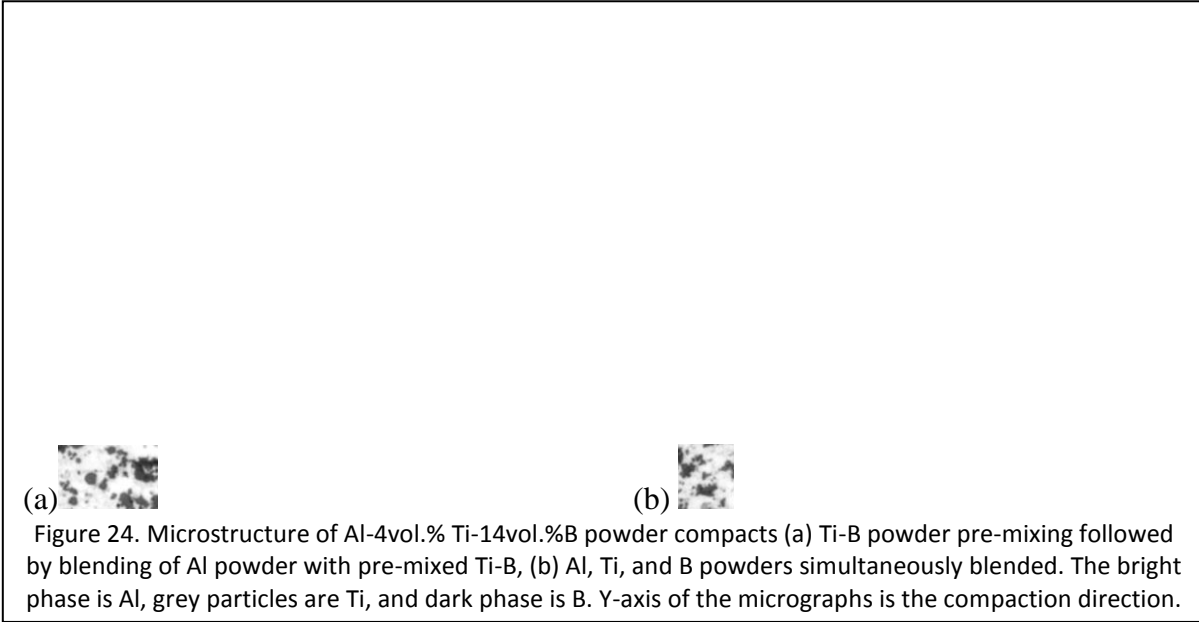
The simulations also correlate extremely well with VISAR traces as shown in Figure 23, capturing the peak velocity and even release-wave events, providing an initial validation for the simulation scheme and physical models employed. The simulated trace even illustrates impactor edge release effects, although simulated trace shows earlier release than the one captured by experimental trace. However, the simulated peak stresses also over-predict the recorded PVDF stress profiles. This may be due to an overly-stiff response from the model, or likely premature failure of gauge. Further experiments are needed for validation.

Figure 23: Simulated (black) particle velocity profiles for 933 m/s experiment show extremely good correlation with non-contact measurement of particle velocity profile captured using VISAR (red).
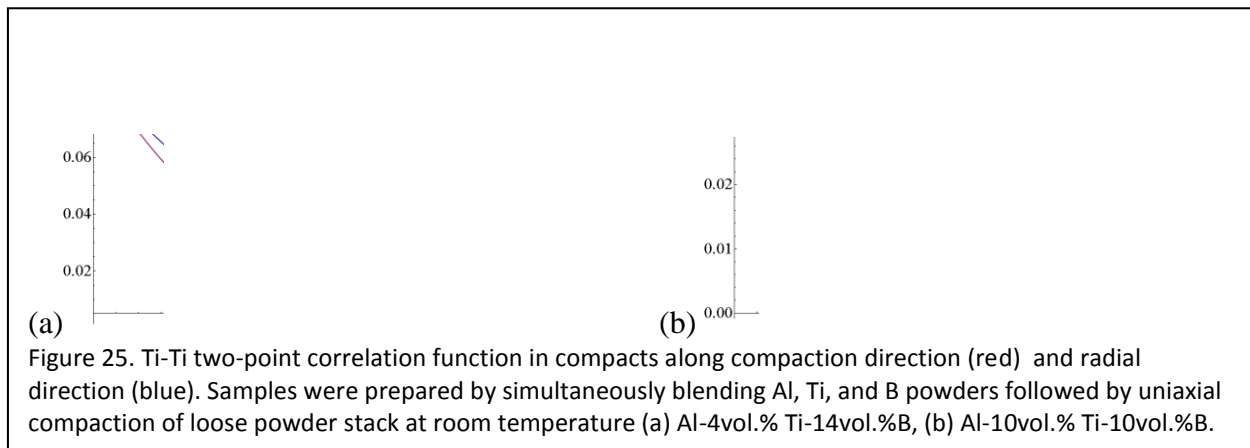
4. Statistical Representation, Reconstruction, and Simulations of Meso-Scale 3-D Microstructures of Reactive Materials

In the powder-processed ternary Ti-B-Al compacts, the relative spatial arrangements of Ti, B, and Al particles are expected to influence the kinematics of impact initiated reactions as well as deformation, fracture, and fragmentation of the constituent particles during high strain rate processes. However, such effects have not been systematically investigated in the past. To understand the effects of powder processing techniques on the microstructural spatial arrangements; to develop and implement the techniques to quantify and mathematically represent such differences in the spatial arrangements; to formulate approaches to incorporate such variations in the spatial arrangements in the simulated realistic multi-phase microstructures; and to simulate the effects of such microstructure variations on the deformation, fracture, and fragmentations of the particles during high strain rate deformation using realistic simulated microstructures, a series of experiments were performed. A set of Al-Ti-B specimens having a range of compositions were prepared using two different powder mixing routes. In one set of specimens, first Ti and B powders were pre-mixed, and then in the second step, the pre-mixed Ti-B was blended with Al powder and compacted to obtain ternary A-Ti-B compact of different compositions. In the second series of specimens, all three elemental powders (Al, Ti, and B) were simultaneously blended and then compacted to obtain the ternary compact of the same set of compositions. These different powder mixing routes lead to different *spatial arrangements* of the Ti, Al, and B constituents in the compacts having the same volume fractions and size distributions of Al, Ti, and B phases.

25

Figure 24 illustrates microstructures of two such specimens having the same Ti, B, and Al volume fractions, size distributions, and all other first order microstructural properties. In these micrographs, Y-axis is the compaction direction. Both microstructures in the figure appear to be isotropic and with no visible differences in the spatial arrangements of the three phases.

(a)   (b)

Figure 24. Microstructure of Al-4vol.% Ti-14vol.%B powder compacts (a) Ti-B powder pre-mixing followed by blending of Al powder with pre-mixed Ti-B, (b) Al, Ti, and B powders simultaneously blended. The bright phase is Al, grey particles are Ti, and dark phase is B. Y-axis of the micrographs is the compaction direction.
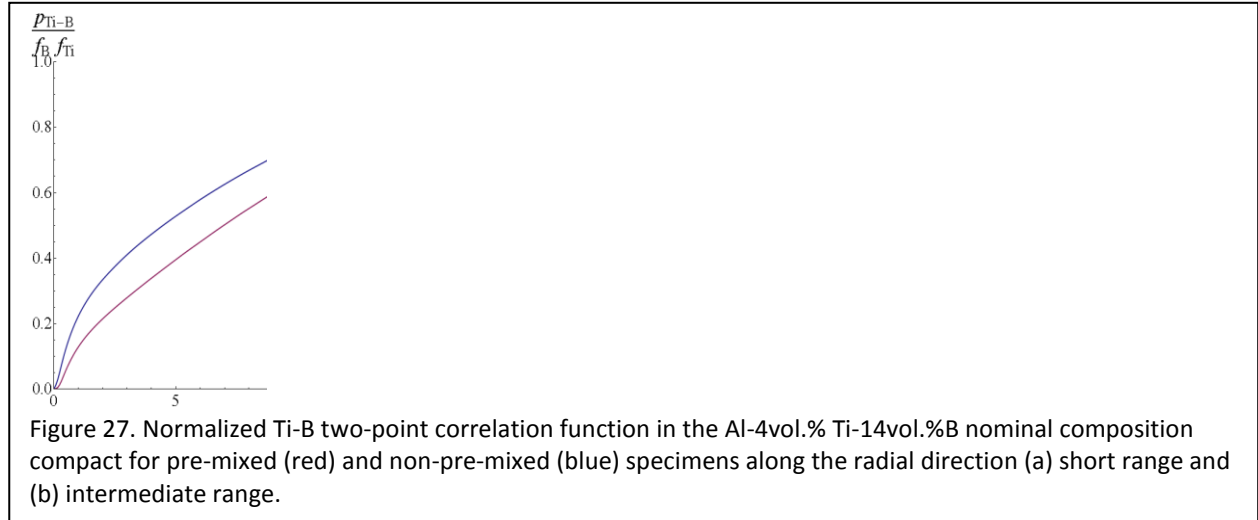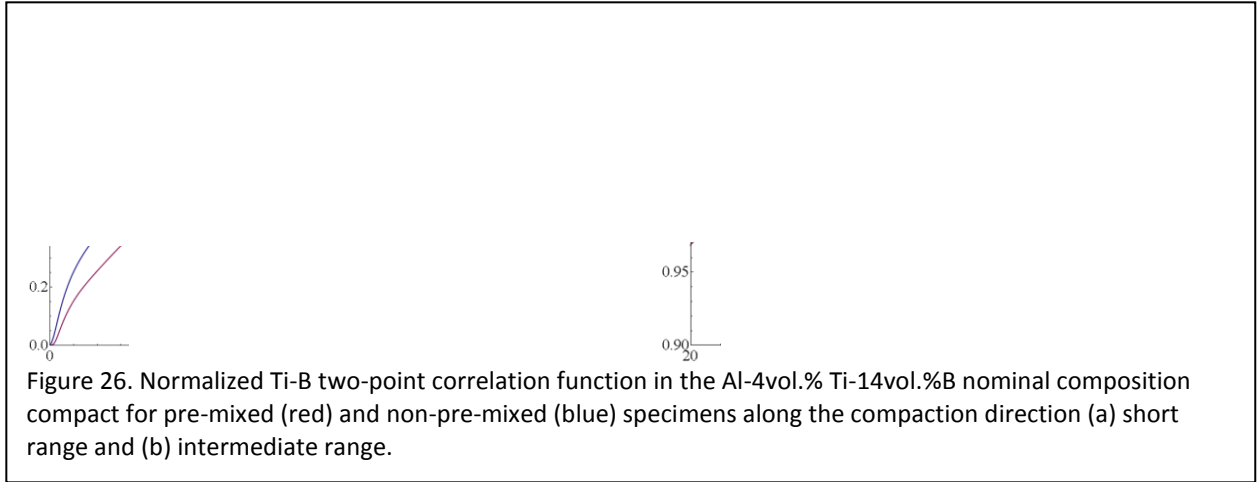
However, quantitative measurements of microstructural two-point correlation functions clearly reveal that (i) there is anisotropy of spatial correlations in these microstructures, and (ii) spatial correlations among Ti, B, and Al constituents are indeed different in the two microstructures. Figure 25 depicts the Ti-Ti two point correlation functions in the two powder compacts along the compaction direction and the radial direction (i.e., perpendicular to compaction direction) prepared by simultaneously blending the Al, Ti, and B powders. Interestingly, the two-point correlation functions in the two directions are significantly different.

(a)   (b)

Figure 25. Ti-Ti two-point correlation function in compacts along compaction direction (red) and radial direction (blue). Samples were prepared by simultaneously blending Al, Ti, and B powders followed by uniaxial compaction of loose powder stack at room temperature (a) Al-4vol.% Ti-14vol.%B, (b) Al-10vol.% Ti-10vol.%B.

Similar trends have been observed in the samples of other compositions and processing conditions. Therefore, the process of uniaxial powder compaction induces mild anisotropy in the spatial arrangements of the particles in these microstructures although individual Ti (as well as B) particles have equiaxed morphologies. These differences in the correlation functions along

the compaction and radial directions are probably caused by particle rearrangements during uniaxial powder compaction process *and* uniaxial deformation of Al which leads to plastic flow of Al in the pore spaces of the powder stack that brings the Ti particles closer along compaction direction. The extent of such direction dependent spatial correlations depends on the parameters of the powder compaction processing such as the compaction load and amount of compaction. Such direction dependence of the spatial correlations may in turn affect the performance of the energetic materials.

Different powder mixing routes (pre-mixing of Ti and B versus simultaneous mixing of Al, Ti, and B powders) also affect the spatial arrangements and correlations represented by the correlation functions. Figure 26 depicts normalized[1] Ti-B two-point correlation functions for the Al-4vol.% Ti-14vol.%B compacts along the <u>compaction</u> direction at short range and intermediate range and Figure 27 depicts the corresponding behavior along the <u>radial</u> direction.

Figure 26. Normalized Ti-B two-point correlation function in the Al-4vol.% Ti-14vol.%B nominal composition compact for pre-mixed (red) and non-pre-mixed (blue) specimens along the compaction direction (a) short range and (b) intermediate range.

Figure 27. Normalized Ti-B two-point correlation function in the Al-4vol.% Ti-14vol.%B nominal composition compact for pre-mixed (red) and non-pre-mixed (blue) specimens along the radial direction (a) short range and (b) intermediate range.

---

[1] Normalized Ti-B two-point correlation function is obtained by dividing the absolute two-point correlation function by the product of the volume fraction of Ti and B, f_{Ti} and f_B. The normalized Ti-B correlation function approaches one as the distance r goes to infinity
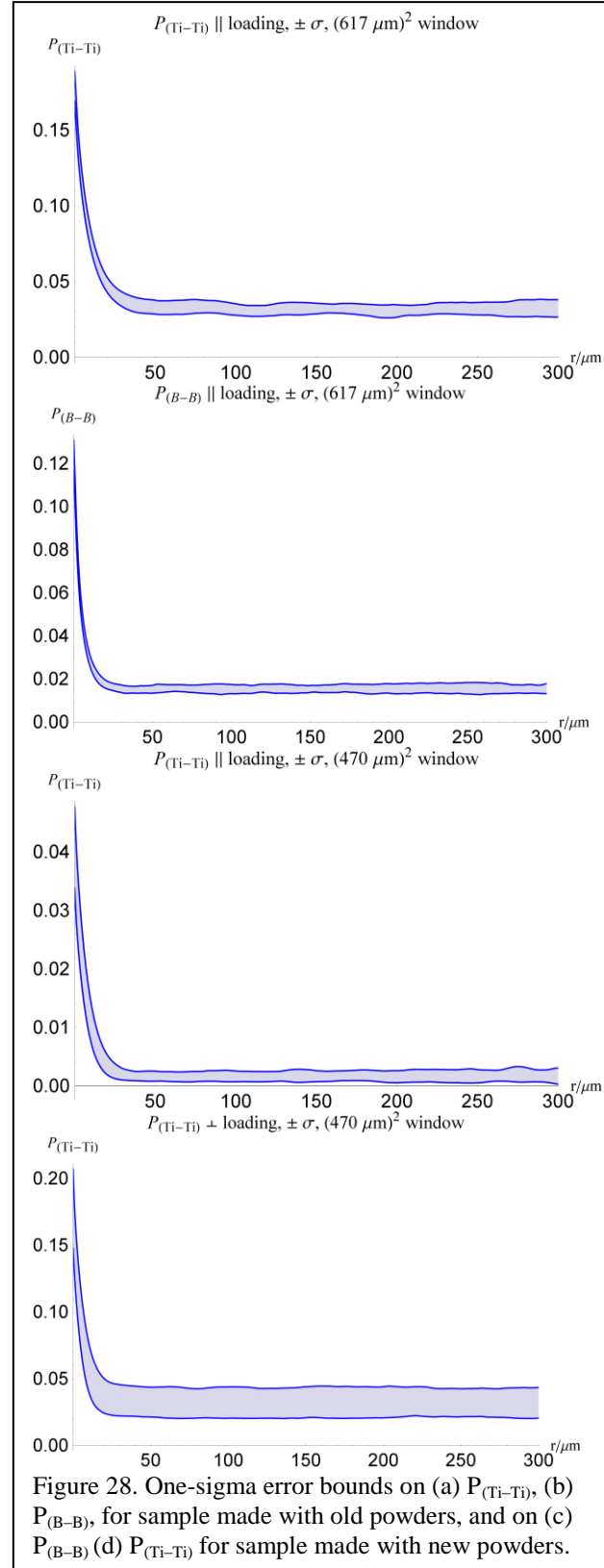
Note that the two-point correlation functions nicely capture the differences in the Ti-B spatial correlations resulting from the two different powder mixing routes: in the compaction as well as radial direction the normalized two-point function probability for the "pre-mixed" compact (red curve) is consistently lower than that for the compact where the Al, Ti, and B powders are simultaneously mixed (blue curve) up to the distances of 20 μm indicating enhanced repulsion between Ti and B at short distances. This is likely to be due to larger extent of agglomeration of the fine B particles in the "pre-mixed" compact. The data on B-B, Ti-Ti, and Al-B two-point correlation functions and lineal path probability distributions are consistent with these trends. Such data sets are crucial for development and validation of the techniques for simulations of realistic multi-phase 3D microstructures where the simulations can mimic subtle variations in the spatial correlations of the constituents arising from the variations in the processing conditions such as powder mixing routes.

As noted in the above results, for given constituent elemental powders, the relative spatial arrangements of Ti, B, and Al particles are expected to influence the kinematics of impact initiated reactions as well as deformation, fracture, and fragmentation of the constituent particles during high-strain-rate processes. The size and shape characteristics of the powder also influence the said processes. We have also developed a complete set of tools to simulate realistic microstructures in three dimensions for the full range of processing conditions in use in impact experiments (i.e. varying compositions, varying anisotropy as determined by the extent of densification, and for two different sets of powders). These simulated microstructures have the same statistics (within measurement error) as the real specimens, thus suggesting that the simulations produce reliable approximations of the real microstructures for use in impact simulations. In addition, our microstructure-simulation toolbox can simulate hypothetical microstructures that differ from the realistic microstructures in one or more parameters that closely correspond to intelligible shape characteristics of the microstructure or spatial arrangements in it.

4.1 Characteristics of real microstructures

After careful examination of all available real microstructures the following three salient conclusions emerge: (i) all microstructures exhibit significant long-range heterogeneities; (ii) there are no statistically significant differences between the microstructures of premixed powder-mixture compacts (i.e. when Ti and B are mixed together first and then blended with Al) and non-premixed compacts (i.e. when all powders are mixed together at the same time); and (iii) all microstructures show marked anisotropy, such that there is a significant difference between the direction parallel and perpendicular to loading. To illustrate the point about heterogeneities, Figure 28 shows two examples each from an old-powder specimen[2] and a new-powder specimen, illustrating the one-standard-deviation range over which the two-point correlation function lies when calculated over tens of different small microstructure windows taken out of a large montage. Only such a calculation can reveal long-range heterogeneities in the microstructure. Since the correlation function at any given r is seen to follow a normal distribution, there is a roughly a 68% chance that a randomly chosen window of the size indicated out of the montage will have a correlation function lying within the band shown.

Simulated microstructures (which typically have similar window sizes) can only be expected to match the real microstructure in two-point correlations to about the same error. Fig. 29 plots the correlation functions along two directions (parallel to, and perpendicular to, loading)

Figure 28. One-sigma error bounds on (a) $P_{(Ti–Ti)}$, (b) $P_{(B–B)}$, for sample made with old powders, and on (c) $P_{(B–B)}$ (d) $P_{(Ti–Ti)}$ for sample made with new powders.

---

[2] Throughout, "old powders" refers to crystalline titanium (Cerac 325-mesh) and boron particles (Alfa-Aesar), and "new powders" refers to sponge (crystalline) titanium (~ 20 μm) and amorphous boron (< 5 μm). The aluminum used for the specimens was Valimet H2 (< 6 μm).

29

on the same plot of a microstructure of (a) old-powder compact and (b) new-powder compact. The parallel-direction correlation function consistently has lower slope at 0, as would be expected if particles reoriented during compression, in every microstructure examined.

4.2 The Simulation Method

Simulations use real particle morphologies extracted from reconstructions of volumes of real binary microstructures (Al–Ti and Al–B), with the exception of new boron particles that proved too small to be accurately segmented even at the highest resolutions in optical microscopy. Hence, the boron particle shapes are simulated based on observed and known size and shape characteristics. The same problem prevented us from obtaining accurate segmentations of ternary images for characterization. Fig. 30 shows some examples of Ti and B particles from this new library. The new library supplements the old library of particles of old powders of Ti and B.
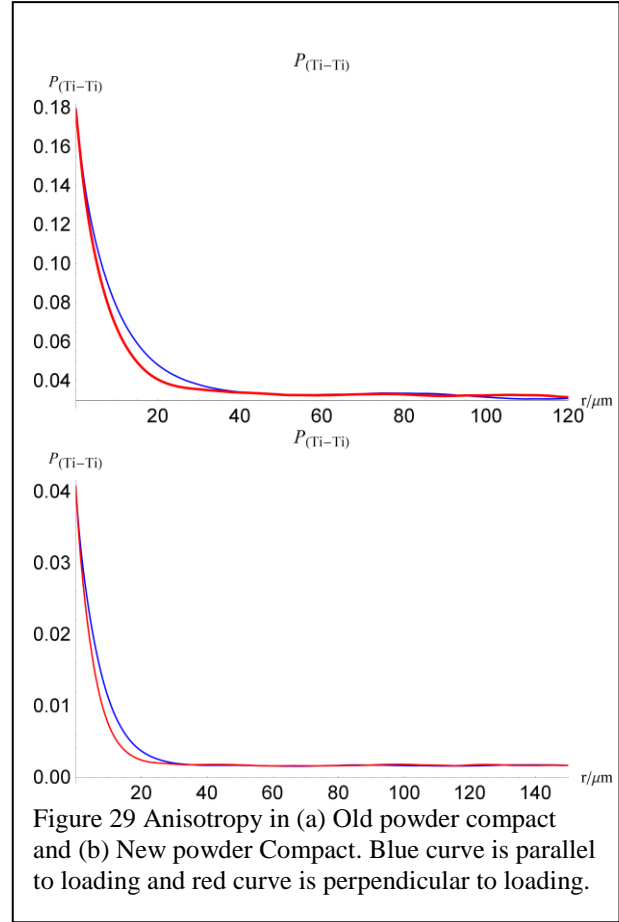

Figure 29 Anisotropy in (a) Old powder compact and (b) New powder Compact. Blue curve is parallel to loading and red curve is perpendicular to loading.
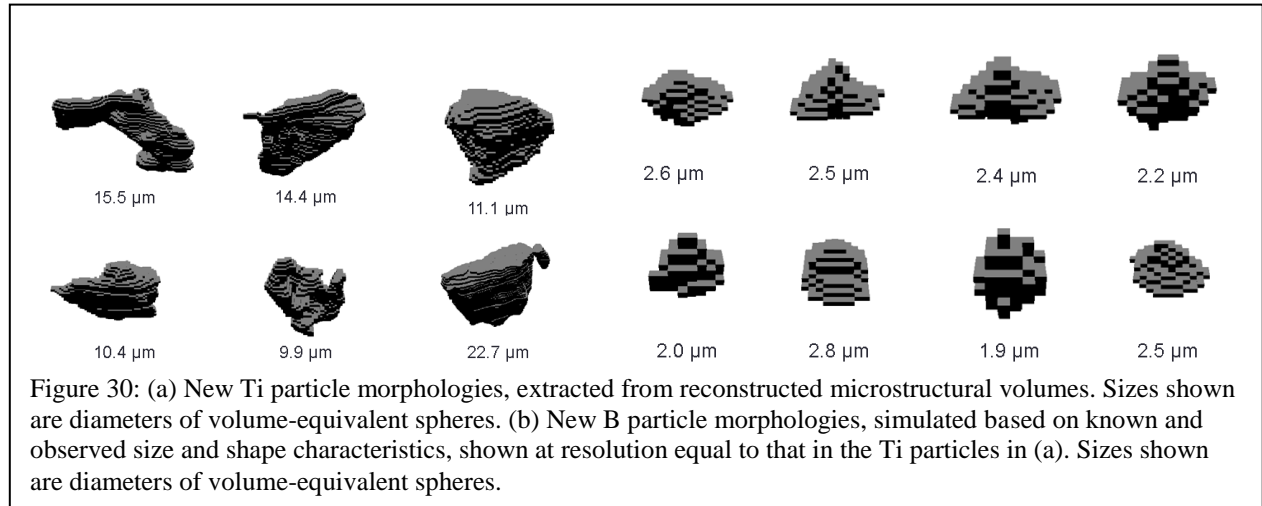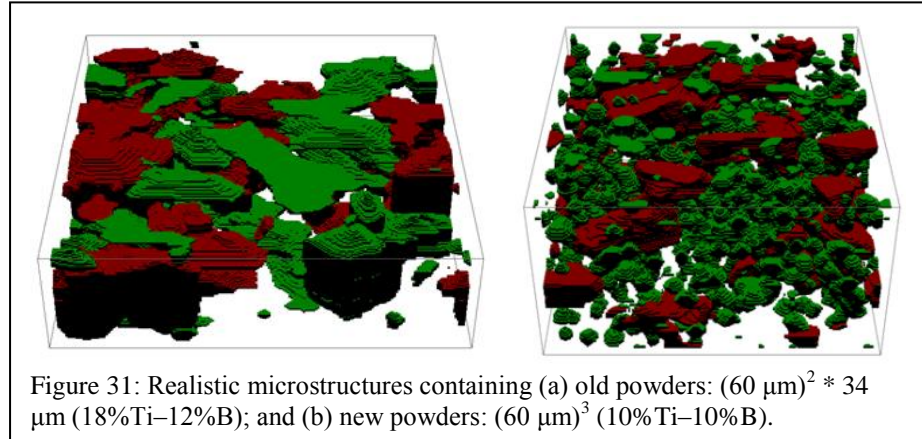

Figure 30: (a) New Ti particle morphologies, extracted from reconstructed microstructural volumes. Sizes shown are diameters of volume-equivalent spheres. (b) New B particle morphologies, simulated based on known and observed size and shape characteristics, shown at resolution equal to that in the Ti particles in (a). Sizes shown are diameters of volume-equivalent spheres.

The simulation method developed is a Monte Carlo method, running a Metropolis simulation within a simulated-annealing framework. It starts out with loading the appropriate libraries of particles of the right dimension (since simulations can be for 2-D or 3-D microstructures), asks for the target volume fractions and particle-selection criteria, if any (based on size and/or shape). After selecting the set of particles (a random set that satisfies all

30

the specifications), it asks for the target distance metric, which controls clustering. This metric is ignored for real-microstructure simulation (more on this below). Then it asks if the particles need to be reoriented to create a certain level of anisotropy. We found that the anisotropic real microstructures could be simulated simply by rotating the set of particles by a set amount calculated as a linear function of porosity. The rationale for linking anisotropy to porosity is that a greater porosity implies less particle rotation during compaction, since the height of the loose powder mixture is reduced by a smaller amount. From measurements, we know that full densification (achieving roughly 95% of theoretical density) requires about 40% reduction in height of the loose powder during compaction. We surmise that the degree of particle rotation is a linear function of the fractional reduction in height. Since no microstructures can be obtained for highly porous samples (due to lack of structural integrity for metallographic observation), this assumption cannot be experimentally tested. The Metropolis simulation places particles on a grid at the start, and through random translations from that initial configuration, the microstructure evolves to meet user specifications. The translations initially are purely random (i.e. there is a high "temperature" in the simulated anneal), but then become increasingly the kind that lower the "energy" (a function of the particle positions that assigns lower values to configurations closer to user specification) by tending to reject "energy"-raising translations. The energy function for simulating real microstructures is one that penalizes overlaps; for simulating clustered microstructures, it also penalizes deviation from the desired distance metric (more on this later). The simulation stops when "energy" has reached a low plateau. Fig. 31 shows two example of 3-D microstructures—one old-powder and one new-powder compact. Fig. 32 shows a comparison of two-point correlation functions between simulated and real microstructures for one composition each of old-powder and new-powder specimens. The good match suggests that the simulated microstructures are good approximations to the real microstructures.

Figure 31: Realistic microstructures containing (a) old powders: $(60\ \mu m)^2 * 34$ μm (18%Ti–12%B); and (b) new powders: $(60\ \mu m)^3$ (10%Ti–10%B).
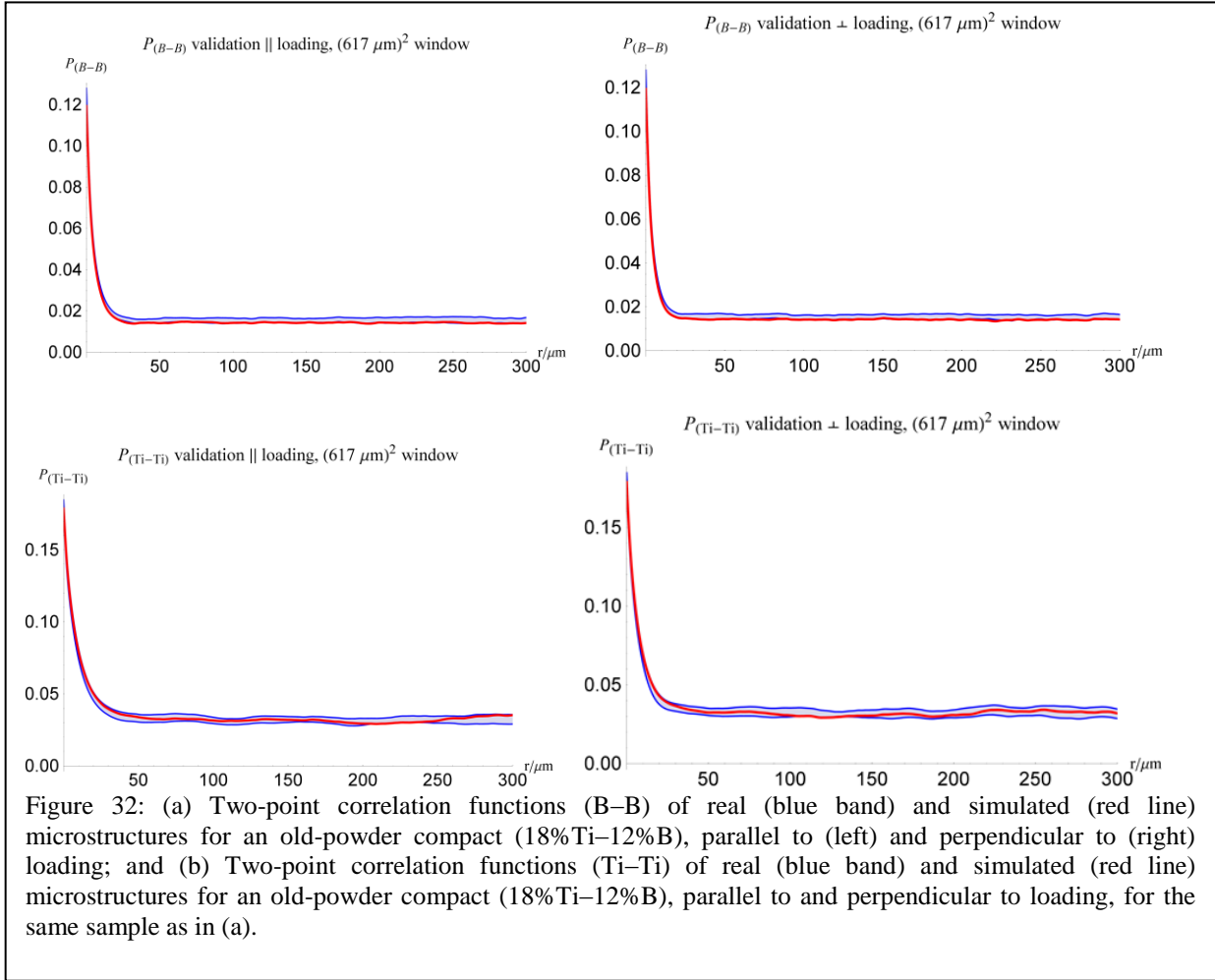
Figure 32: (a) Two-point correlation functions (B–B) of real (blue band) and simulated (red line) microstructures for an old-powder compact (18%Ti–12%B), parallel to (left) and perpendicular to (right) loading; and (b) Two-point correlation functions (Ti–Ti) of real (blue band) and simulated (red line) microstructures for an old-powder compact (18%Ti–12%B), parallel to and perpendicular to loading, for the same sample as in (a).

4.3 Parameterization of Shape

Invariant Moments: Since material behavior is clearly sensitive to the shapes of constituents, it is very helpful to control parametrically the shapes of powders in the specimen. In the realistic simulated microstructures, the shapes must be randomly chosen from the particle library. But in hypothetical microstructures, it is helpful to select them by some shape-sensitive criteria. Toward this end, we added shape-selection capability to the simulation toolbox that uses seven invariant moments to characterize a particle's shape (calculated from the set of central moments of the particle image up to order three). A given shape (such as a circle or an ellipse with a certain eccentricity) always has the same moments, regardless of the size or orientation. Though the numbers are themselves not easily interpretable, each set of moments (thus each particle shape) is a point in 7-dimensional space, and the set of these points can be subjected to standard clustering analysis to classify the available shapes into n classes, where the user chooses n. In the simulation, rules can be specified as to which shapes and in what proportion should be used in the simulation. Fig. 33 shows three Ti particles each from three of the shape classes obtained by setting n to 5.

Circularization/Spheroidization of Shapes: We also added the ability to *change* existing shapes to make them some percentage circular (2-D particles) or spherical (3-D particles), based on image processing relying on distance transforms. The original shapes are considered 0% circular/spherical, and a circle/sphere of the same area/volume as the particle represents 100% on the scale. This provides a way to test, say, the influence of flakiness of shape on deformation and reaction behavior, since flake particles would have distinctly different invariant moments. Going from 0% to 100% circular, the perimeter (or surface area in 3-D) decreases. Fig. 34 shows some points on the scale for a randomly chosen 2-D titanium particle.
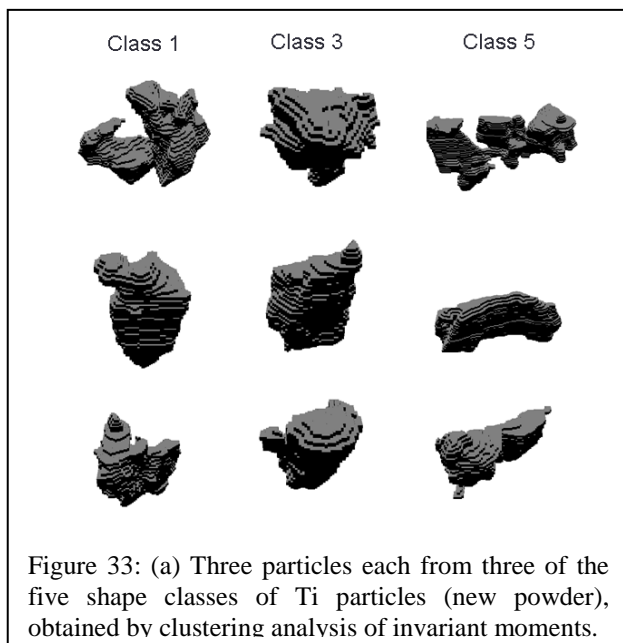

Figure 33: (a) Three particles each from three of the five shape classes of Ti particles (new powder), obtained by clustering analysis of invariant moments.

Figure. 34. A randomly chosen Ti particle, circularized to varying degrees, starting with original particle (leftmost) to 90% circular (extreme right) in increments of 10%. The area is held constant.

4.4 Parameterization of Clustering

For a microstructure consisting of various shapes and sizes, an nth-nearest-neighbor distribution of centroids does not adequately describe actual surface–surface distances between particles. We therefore formulated two metrics: minimum *A*-to-*B* and minimum *B*-to-*A* distance distributions for two particle phases *A* and *B*. The *A*-to-*B* distribution is the probability density function of random variable representing the distance to nearest surface point on *B* from a randomly chosen surface point on *A*; likewise for *B*-to-*A*. Moments of these distributions can then be used to characterize clustering or as targets in simulation by incorporating them into the "energy" function. Fig. 35 shows two microstructures simulated in this manner, with the difference in
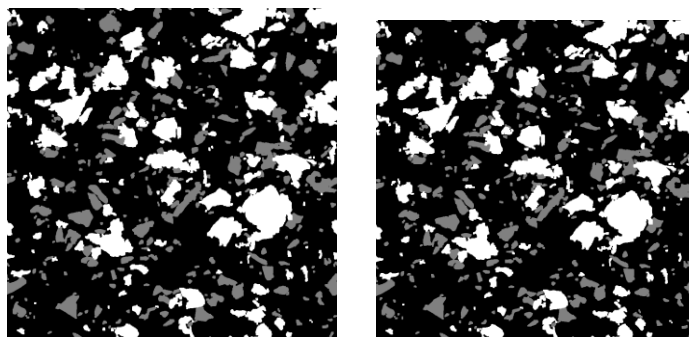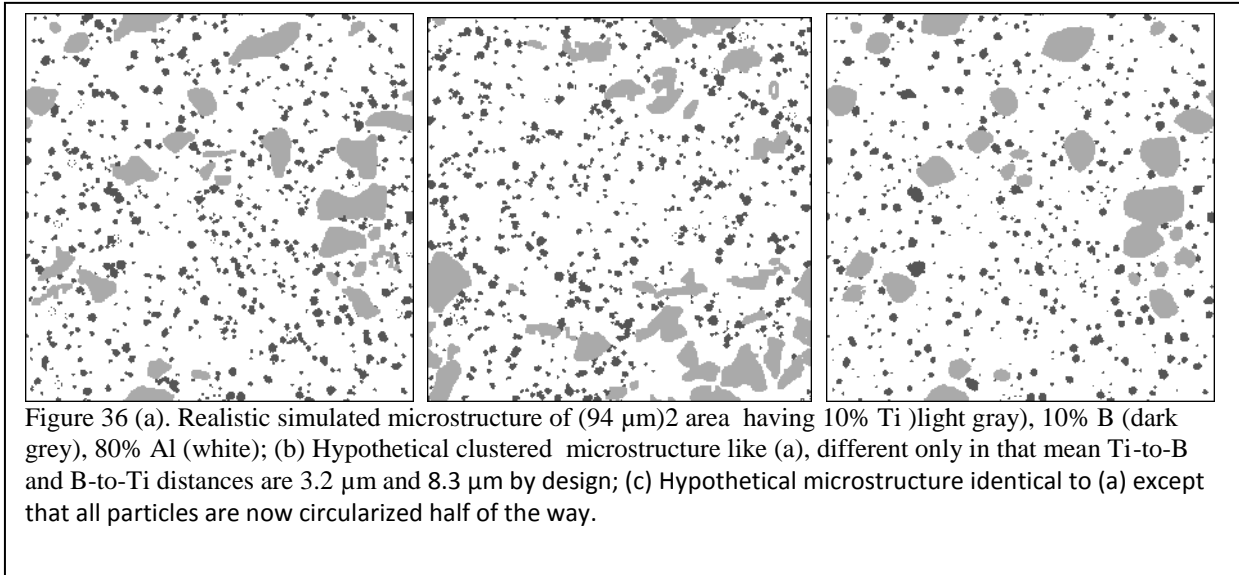

Figure 35. Two simulated microstructures with different target distance metrics, 313.5 μm^2 in area. White = Ti; gray = boron. (Left) Mean Ti-to-B distance (left) = 7.6 μm, Mean B-to-Ti distance = 7.8 μm. (Right) Mean Ti-to-B distance (left) = 11.0 μm, Mean B-to-Ti distance = 10.2 μm.
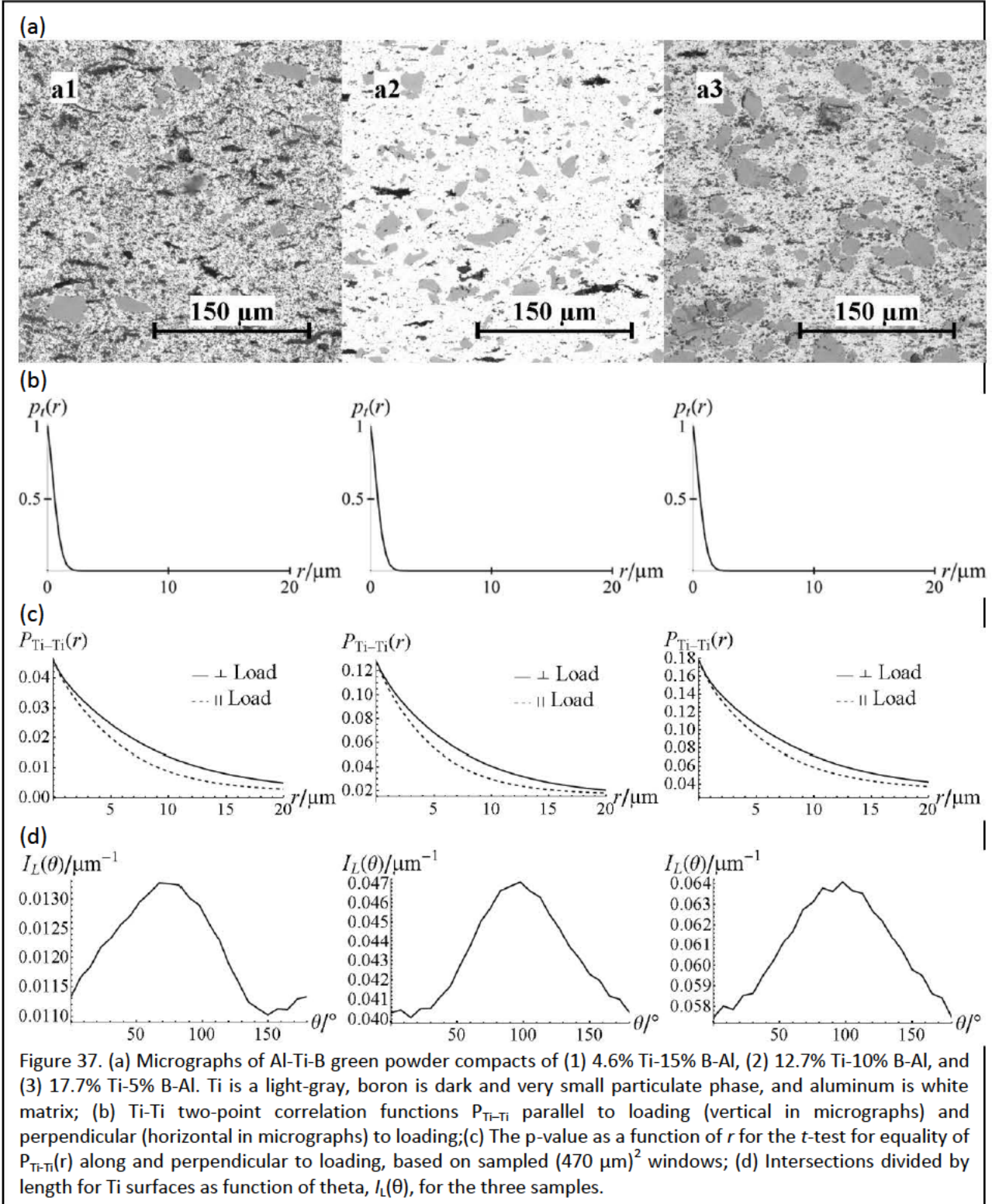
clustering apparent. All parameterizations are now available in 3-D and 2-D, although it is easier to illustrate them in two dimensions. They may be used in statistical design of experiments (using impact simulations) to disentangle the effects of various microstructural attributes.

4.5 Design of Experiments (DOE) for Delineating Effects of Microstructural Parameters

The parametric investigation of microstructural characteristics on impact behavior was extended through a design of experiments effort to delineate the effects of microstructural parameters. We have simulated a set of realistic and hypothetical microstructures for parametric investigation, from which examples follow. In Fig 36(a) is a $(94 \ \mu m)^2$ *realistic* simulated microstructure with crystalline Ti and amorphous B particles, 10% by volume of each. (Titanium is light gray, boron dark gray, and aluminum white.) Fig 36(b-c) are hypothetical microstructures, as described below, of the same composition. For a microstructure consisting of various shapes and various sizes, an nth-nearest-neighbor distribution of centroids does not adequately describe actual surface–surface distances between particles. We therefore formulated two metrics: the minimum A-to-B and the minimum B-to-A distance distributions for two particle phases A and B. The A-to-B distribution is the probability density function of the random variable representing the distance to the nearest surface point on B from a randomly chosen surface point on A; likewise for B-to-A. The realistic microstructure in Fig 36(a) has mean Ti-to-B distance 1.8 μm and mean B-to-Ti distance 5.8 μm. In Fig 36(b) is a hypothetical microstructure with the mean Ti-to-B and B-to-Ti distances 3.2 μm and 8.3 μm by design. We also used a morphological parameter to change: circularity. Our simulation toolbox can change existing shapes to make them some percentage of the 2-D particles circular, based on image processing relying on distance transforms. The original shapes are considered 0% circular, and a circle of the same area has circularity 100%. This provides a way to test, say, the influence of flakiness of shape on impact behavior. Going from 0% to 100% circular, the perimeter (surface area in three dimensions) decreases. Fig. 36(c) is exactly the realistic microstructure of Fig. 36(a), except that all particles are now 50% circular.

Figure 36 (a). Realistic simulated microstructure of (94 μm)2 area having 10% Ti)light gray), 10% B (dark grey), 80% Al (white); (b) Hypothetical clustered microstructure like (a), different only in that mean Ti-to-B and B-to-Ti distances are 3.2 μm and 8.3 μm by design; (c) Hypothetical microstructure identical to (a) except that all particles are now circularized half of the way.

Numerical Proof of Anisotropy of Compact Microstructures: We rigorously analyzed the real 2-D compact microstructures for quantification of its features. Quantitative proof of anisotropy between the loading direction and the perpendicular direction, based on *t*-tests on two-point correlations in perpendicular directions, is now available. Fig 37 shows (a) the

Figure 37. (a) Micrographs of Al-Ti-B green powder compacts of (1) 4.6% Ti-15% B-Al, (2) 12.7% Ti-10% B-Al, and (3) 17.7% Ti-5% B-Al. Ti is a light-gray, boron is dark and very small particulate phase, and aluminum is white matrix; (b) Ti-Ti two-point correlation functions P_{Ti-Ti} parallel to loading (vertical in micrographs) and perpendicular (horizontal in micrographs) to loading;(c) The p-value as a function of r for the *t*-test for equality of $P_{Ti-Ti}(r)$ along and perpendicular to loading, based on sampled $(470 \ \mu m)^2$ windows; (d) Intersections divided by length for Ti surfaces as function of theta, $I_L(\theta)$, for the three samples.

microstructures of three specimens made with the same elemental powders, (b) the two-point correlation functions in the two directions, (c) the *t*-test as a function of distance, and (d) the intersections per length as a function of angle made with the perpendicular to the loading direction. Since the two-point correlation functions are mathematically constrained to be equal at 0, the *t*-test fails to reject the hypothesis that the two functions are equal there. But the p-value quickly drops to nearly 0 (i.e., the functions are unequal) with increasing *r*. This is exactly what is expected if there is anisotropy of Ti surfaces, because at low *r*, the two-point correlation function is dominated by the morphology of the microstructure and at large *r* by spatial features. We have submitted a manuscript for publication in *Scripta Materialia* summarizing these findings and reporting on possible implications for processing of powders.

5.   Non-equilibrium Molecular Dynamics Simulations of Shocked Ni/Al Nanolaminates

5.1   Simulation of Ni+Al Nanolaminates

Non-equilibrium molecular dynamics simulations were conducted on Ni/Al laminates in order to investigate, at the atomic level, a system that has been well-studied experimentally by Specht and Thadhani.[46] Simulations were performed using the SPaSM (Scalable Parallel Short-range Molecular Dynamics) software developed at Los Alamos, using a time step of 0.2 fs. Interatomic forces were computed using the embedded atom method (EAM) potential developed by Purja Pun and Mishin in 2009.[47] The shock (longitudinal) dimension is *z*, and periodic boundary conditions were employed in the *x* and *y* dimensions. The model systems were constructed by building both the Ni and Al fcc layers with the 111 crystallographic direction parallel to the *z* axis. After minimizing the potential energy, the system was equilibrated at 300 K for 0.6 ps. The NEMD simulation was performed with an atomistic piston located at *z* = 0, with a thickness approximately equal to the cutoff distance (6.3 Å) of the potential. The initial velocities of the remaining atoms are the equilibrated velocities minus the piston velocity (*i.e.*, the piston is stationary and all atoms initially move in the –*z* direction). The piston velocities ranged from 0.5 to 1.0 km/s.

The systems studied consisted of a 1:1 stoichiometric ratio of Ni and Al, with alternating layers of the two metals. The interfaces of the layers were planar, and we varied the angle (0° and 90°) between the interfaces and the shock direction. The perpendicular (⊥) simulations are similar to simulations performed by other researchers,[48] while simulations with the shock running parallel (∥) to the interfaces have not been conducted previously. For the ⊥ simulations, we used two system configurations each containing ~13.4 million atoms. The first configuration consisted of 3 bilayers, with the Ni layer 313 nm thick and the Al layer 496 nm thick. The second configuration consisted of 6 bilayers, each one half as thick as in the first configuration. In the ∥ case, two system sizes were used in order to establish the size dependence of the results. The smaller ∥ system contained 61.6 million atoms, and the larger ∥ system contained 255.7 million atoms. Both configurations contained a single bilayer, which,

in the larger system, consisted of a 393-nm thick Ni layer and a 620-nm thick Al layer. More information on the initial system dimensions is given in Table III.

Table III. System dimensions.

Interface direction	layer thickness ratio [a]	$N_{bilayers}$	$N_{interfaces}$	Ni layer thickness nm	Al layer thickness Nm	thickness x dimension nm	thickness y dimension Nm	length z dimension nm	# Ni atoms	# Al atoms
⊥	1.0	2	3	78.22 [a]	123.92 [a]	6.67	11.56	404.28	1,119,744	1,117,071
⊥	2.0	6	11	156.44 [a]	247.84 [a]	6.67	11.56	2425.67	6,718,464	6,702,430
⊥	4.0	3	5	312.88 [a]	495.67 [a]	6.67	11.56	2425.67	6,718,464	6,702,430
||	0.6	1	2	47.40 [b]	74.73 [b]	122.14	11.81	595.15	30,164,400	31,449,600
||	5.0	1	2	393.43 [b]	620.29 [b]	1013.73	11.81	297.58	125,182,260	130,515,840

[a] example: the larger of the || systems has layers 5 times as thick as the smallest ⊥ system
[b] z dimension
[c] x dimension

For some small systems, simulations were continued after the shock state was reached. This is often referred to as a 'cook-off' simulation and is carried out at fixed volume and total energy (micro-canonical ensemble). The initial conditions for the cook-off runs were taken from the NEMD shock trajectories at the point in time at which the shock wave reaches the free surface of the material. The precise trajectory point chosen for the initial conditions was the time slice at which the longitudinal acceleration for the final 0.66 nm of material was closest to zero. The material comprising the piston in the shock run was kept frozen in the cook-off simulation, and an additional 6.3 Å of material was frozen at the other (free) surface. Hence, the system modeled in the cook-off simulation is the shocked state of the original system with 6.3 Å of material clamped at each longitudinal end. Our procedure follows closely the method developed by Sewell and coworkers.[49]

Results and Discussion: A summary of our NEMD simulation results is given in Table IV. The final time is the time at which the fully shocked state is reached (when the shock wave reaches the free surface opposite to the piston). Note that the final pressure is also the peak pressure. The final two columns in Table IV give a measure of the degree of alloying (mixing of Ni and Al) that occurs. Ni/Al mixing is quite small in our simulations due to the short timescales and the fact that the initial model system is composed of perfect crystals and planar

intermetallic interfaces with relatively low potential energies. More details on Ni/Al mixing will be presented later in this section.

Table II. Results from NEMD simulations on Ni/Al nano-laminates.

Interface direction	$N_{bilayers}$	$N_{interfaces}$	u_p	Final P^a	Final T	Final time	Peak T	Final fraction mixed per sq. nm ($\times 10^{-6}$)[b]		% Increase in Mixing	
			(km/s)	(GPa)	(K)	(ps)	(K)	Ni	Al	Ni	Al
⊥	3	5	0.5	8.36	415.6	316.2	505.5	3.1	2.6	9.1	20.0
⊥*	3	5	0.5	8.98	383.9	336.4	438.8				
⊥	3	5	1.0	19.15	696.6	357.0	988.3	4.4	4.1	54.5	100.0
⊥	6	11	0.5	8.88	399.5	343.6	457.6	3.1	2.4	8.3	17.6
⊥*	6	11	0.5	9.49	376.4	374.6	435.9				
⊥	6	11	1.0	20.14	680.2	398.8	888.2	4.5	4.2	58.3	111.8
||	1	2	0.5	8.48	423.0	115.6	436.9	0.9	0.8	28	62
||	1	2	1.0	19.64	691.4	101.8	810.3	1.2	1.1	61	116

[a] The final pressure is also the peak pressure. [b] Overall fraction of atoms that have at least 1 neighbor of the opposite metal. The value is the fraction of the total Ni or Al atoms in the system divided by the total interfacial area.

* configuration is piston/Al/Ni/Al/Ni/Al/Ni instead of piston/Ni/Al/Ni/Al/Ni/Al

Figure 38 shows the temperature plotted as a function of time for the ⊥ simulations. Separate simulations were conducted for piston/Ni/Al/… and piston/Al/Ni/… configurations, and the mean temperature for these configurations is shown in Figure 38 as well. Due to the large difference in the compressibility of Ni and Al, the simulation results for these two configurations show striking differences that will be discussed in more detail below. In general, the peak temperature as well as the final temperature of the fully shocked state is higher when the piston is adjacent to a Ni layer. To extend the timescale of the simulation, we clamped smaller systems (2 bilayers, total length in z dimension was 400
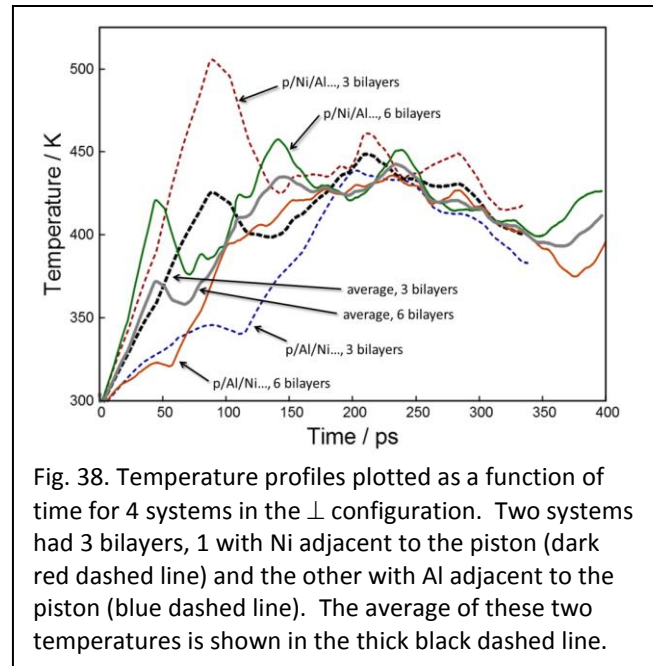

Fig. 38. Temperature profiles plotted as a function of time for 4 systems in the ⊥ configuration. Two systems had 3 bilayers, 1 with Ni adjacent to the piston (dark red dashed line) and the other with Al adjacent to the piston (blue dashed line). The average of these two temperatures is shown in the thick black dashed line.

nm) obtained from NEMD in their shocked states and continued the simulations using equilibrium MD. Results are shown in Figure 39. We did not observe a significant increase in reactivity up to a nanosecond of simulation time. The temperatures from $\perp$ and $||$ simulations are plotted together in Figure 40 as a function of a dimensionless quantity equal to the elapsed time multiplied by the strain rate for the simulation. This allows a direct comparison of simulations with variable longitudinal dimensions. It can be seen that the orange, green and blue lines have similar temperature plots, while the gray stays hot longer. The blue line corresponds to a system with much thinner Ni and Al layers than the other systems. The plot shows that the timescales for heating as well as the peak temperatures are similar for the $\perp$ and $||$ cases if the layer thicknesses are also similar.
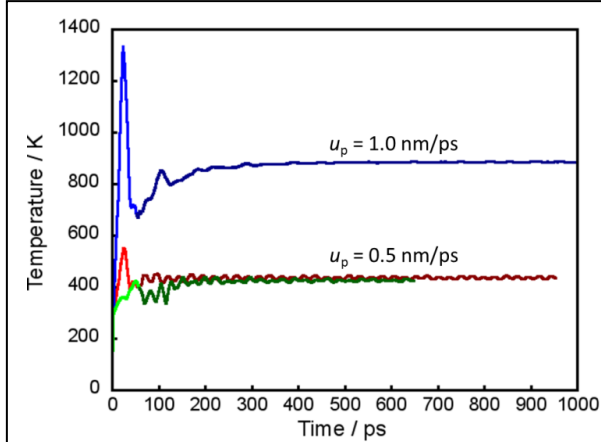

Fig. 39. Temperature plotted as function of simulation time for three systems containing 2 bilayers in $\perp$ configuration. Red and blue lines correspond to systems both with piston/Ni/Al/Ni/Al configurations but different particle velocities (0.5 and 1.0 km/s, respectively). Green line represents a system with piston/Al/Ni/Al/Ni configuration. Solid lines are for systems having 6 bilayers half as thick, with solid gray line being average of the two temperatures.
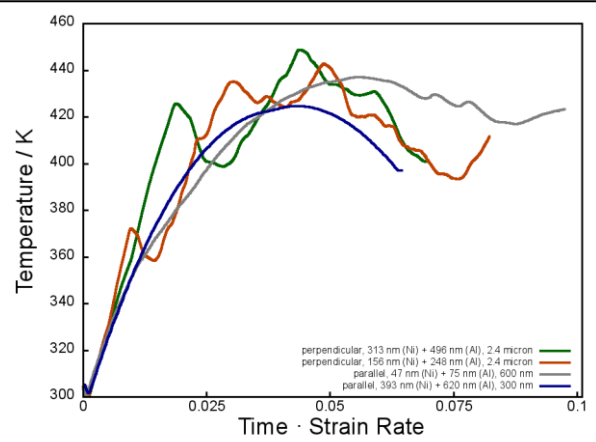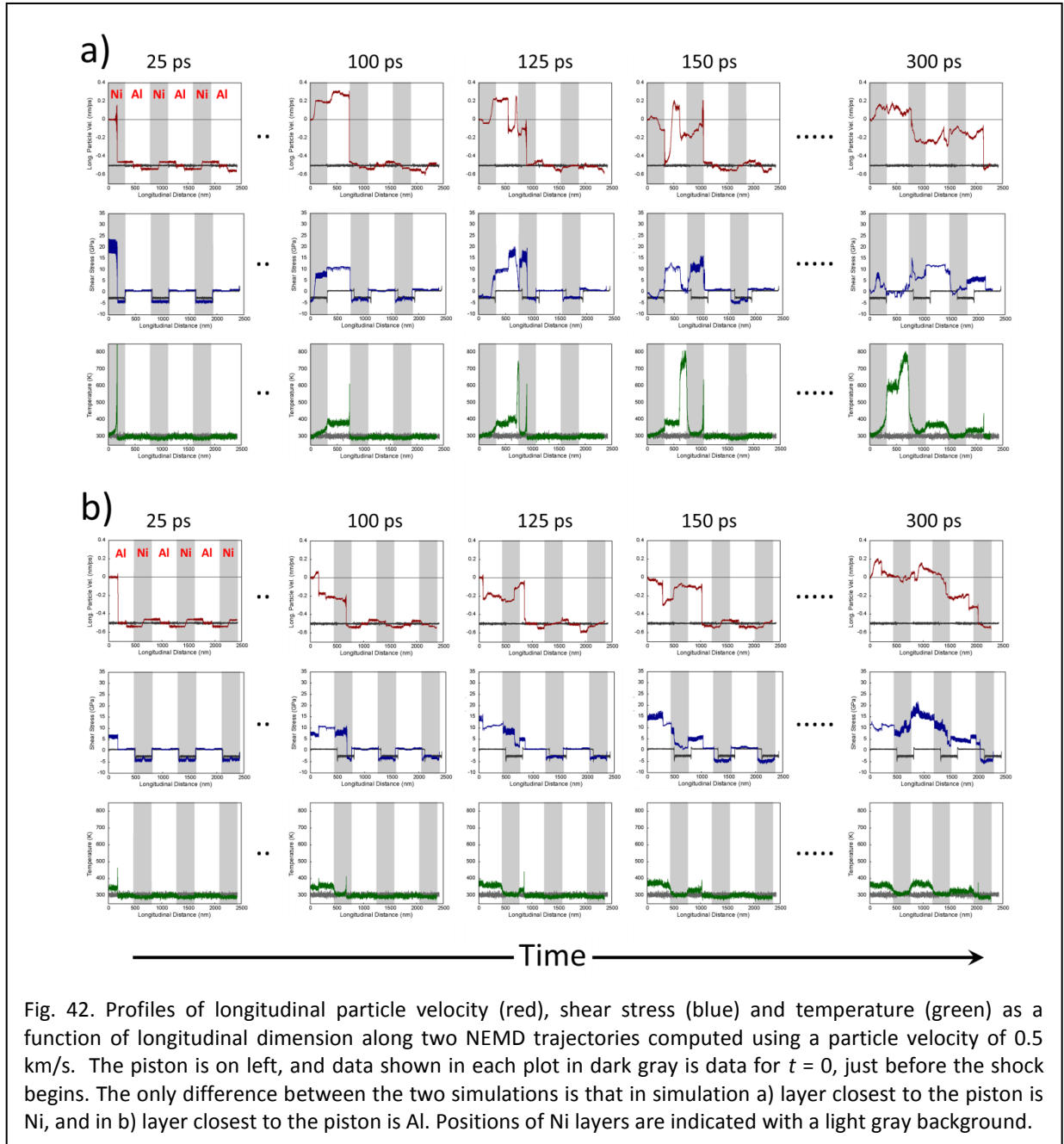
Fig. 40. Temperature plotted as a function of elapsed time multiplied by the strain rate for the system (the abscissa is therefore unitless). The green (orange) line is the average temperature for two simulations, both with 3 (6) bilayers but one with Ni adjacent to the piston and one with Al adjacent to the piston. The blue and gray lines correspond to simulations of systems in the $||$ configuration. See Table I for more information.

Figure 41a shows shear stress, temperature and longitudinal particle velocity profiles as a function of longitudinal dimension for the $\perp$ simulations, respectively. The configuration of the layers is piston/Ni/Al/Ni/Al/Ni/Al. The local quantities were computed in 0.66 nm bins along the z dimension. In the first snapshot ($t = 25$ ps), the wave is about halfway through the first Ni layer and the shear stress is 20 GPa and uniform as a function of distance behind the shock front. The shear stress in the first Ni layer is partially relieved by a reflection wave which begins to propagate back toward the piston when the shock wave reaches the first Ni/Al interface. After 100 ps the wave reaches the second interface (located at ~700 nm). Thereafter, as the longitudinal particle velocity profiles of Figure 37 show, reflection waves become more important as a significant fraction of the Al atoms in bilayer 1 are moving in the opposite direction of the shock front at $t = 125$ and 150 ps. The temperature increase in this layer follows the decrease in stress, and at the end of simulation (not shown) the peak temperature in the Al layer of bilayer 1 is almost 800 K. In contrast, in the Al of bilayer 2, the shear stress is

39

not relieved to the same degree on the timescale of the simulation and the temperature does not climb above 375 K. Figure 42b shows the same simulation results but for a system with a piston/Al/Ni/Al/Ni/Al/Ni configuration of layers. In this simulation, a layer of Al is compressed earliest, and it appears that due to the significantly higher compressibility of Al compared to Ni, the overall response of the system to the shock is much less dramatic than in the simulation described in Figure 42a. The most striking difference between the simulation results is in the temperature profiles at 300 ps. While the simulation with Ni closest to the piston (Fig. 42a) yields a peak Al temperature of 800 K, the same value for the system with Al closest to the piston (Fig. 42b) is less 400 K.

Fig. 42. Profiles of longitudinal particle velocity (red), shear stress (blue) and temperature (green) as a function of longitudinal dimension along two NEMD trajectories computed using a particle velocity of 0.5 km/s. The piston is on left, and data shown in each plot in dark gray is data for *t* = 0, just before the shock begins. The only difference between the two simulations is that in simulation a) layer closest to the piston is Ni, and in b) layer closest to the piston is Al. Positions of Ni layers are indicated with a light gray background.

Snapshots of the local shear stress and temperature for a ‖ simulation are shown in the *x-z* plane in Figure 43. As with all MD simulations reported here, the simulation was conducted with periodic boundary conditions in the transverse dimensions. Heat flares from the interface into the Al, then diffuses and eventually temperature becomes more isotropic in the individual layers. This heating occurs with a very small of amount of Ni/Al mixing.
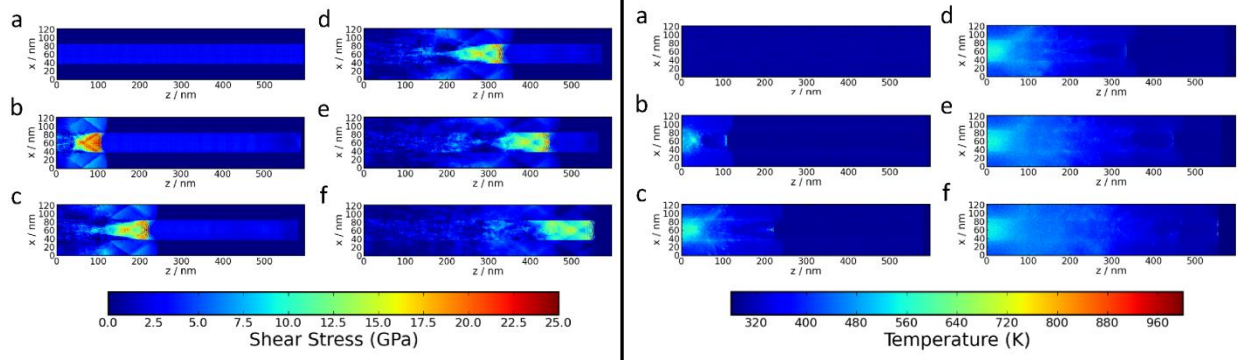

Figure 43. Shear stress and temperature profiles along an NEMD trajectory (thickness in *x* dimension is 122 nm) as a function of longitudinal and transverse dimensions. The piston is on the left at *z* = 0, and the piston velocity was 0.5 km/s. The snapshots were taken at a) 0 ps, b) 16.8 ps, c) 33.6 ps, d) 50.4 ps, e) 67.2 ps, and f) 84.0 ps.

The temperature profiles for a simulation with transverse dimension ~1 micron in thick (Fig. 44) shows that heat 'jets' from the interface laterally into the Ni layer. High shear stress begins when adjacent jets interact, which suggests a dependence of reaction rate on bilayer thickness.

Alloying was quantified from our results by monitoring the identity of the nearest neighbors of each atom in the system. The final fraction of atoms that mixes, as well as the percent increase from the start of the simulation is listed for each trajectory in Table III. Figure 45 shows the time dependence of another measure of the degree of intermetallic mixing.   In this
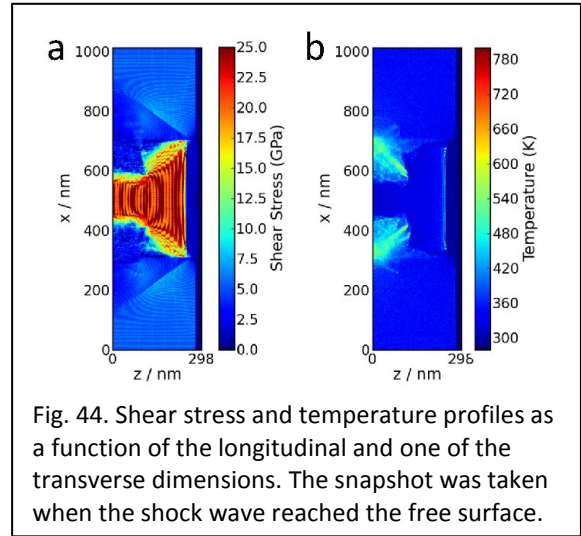

Fig. 44. Shear stress and temperature profiles as a function of the longitudinal and one of the transverse dimensions. The snapshot was taken when the shock wave reached the free surface.

graph we plot the average number of nearest neighbor atoms of the opposite metal for atoms with at least one neighboring atom of the opposite metal. Since the timescales of our simulations are short, only a very small amount of mixing is observed. Cookoff trajectories computed for nearly a nanosecond did not show a significant increase in reactivity (see Figure 39). Figure 46 shows the Ni and Al surfaces at each interface for the final shocked state of the perpendicular system. The layers are separated in the figure in order to show the degree of mixing. What is most interesting about these results is that the planarity of the second interface is disrupted more than the first. We believe this is due to the fact the shock wave moves from the material with higher compressibility into the material with lower compressibility at interface 2, opposite the case for layer 1.
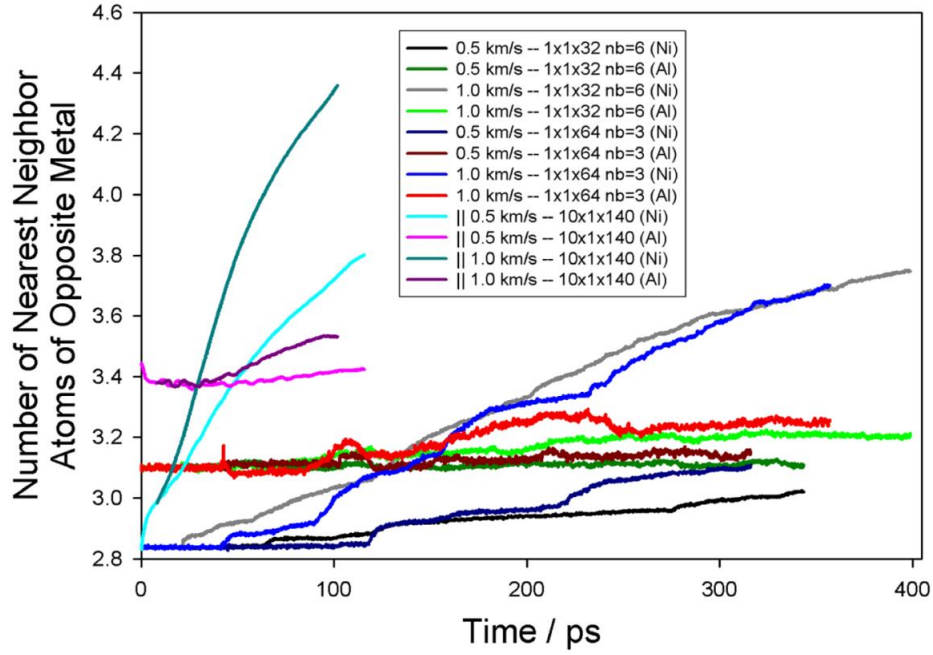
41

Fig. 45. Degree of mixing of each metal (Ni and Al) with the other metal. The quantity plotted versus time is the average number of nearest neighbor atoms that are of the opposite metal type. Only atoms with at least 1 neighbor of the opposite metal are included in the average.
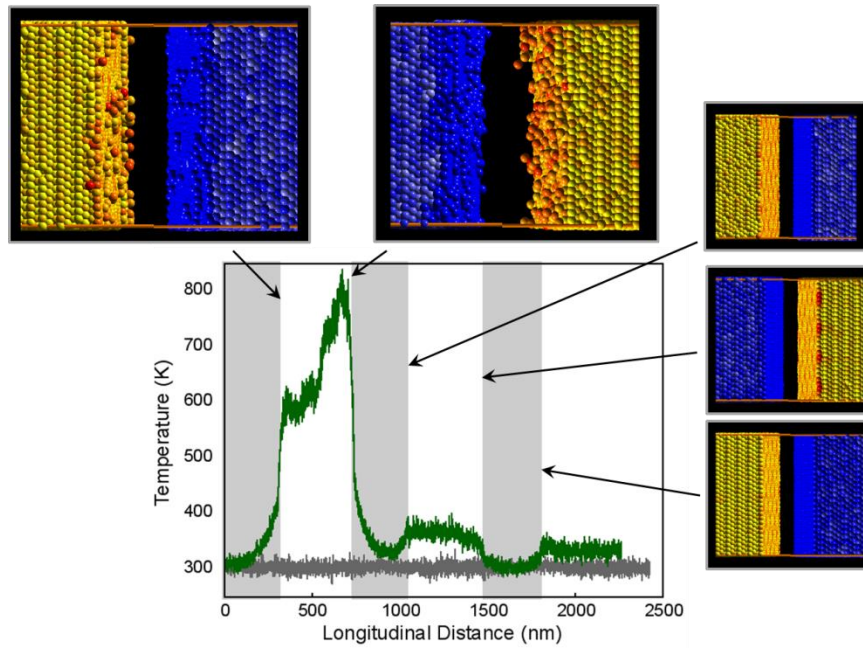

Fig. 46. Snapshots of five interfaces for simulation conducted with u_p = 0.5 km/s. All snapshots pertain to the fully shocked state of the system. The shock traveled from the left to right.

5.2   Toward MD Simulation of Shock-Induced Chemical Reactions of Titanium and Boron

Molecular dynamics (MD) simulations using a reactive force field were used to study the shock-induced interfacial chemistry in Ti/B nanocomposites. MD trajectories were computed using the LAMMPS software, and interatomic forces calculated with the ReaxFF reactive force field. Due to the complexity of the ReaxFF potential form and the high computational cost of computing forces with this force field, we constrained the Ti/B system to evolve according to the Hugoniot conservation relations using either the NPzzHug or MSST techniques. The usual method for computing shock properties of an atomistic model system is to perform NEMD simulations. The drawback of this technique is that the time duration of the simulation is proportional to the system size. As a result, chemical processes that occur on a long timescale cannot be modeled with standard NEMD techniques. The NPzzHug and MSST methods aim to decouple the time duration of the simulation from the size of the system. Both methods allow studies of the chemical reactivity of a material as a function of the strength of mechanical impact (external pressure in the case of NPzzHug, and shock velocity in the case of MSST). The first task in this project was the development of a force field.

The ReaxFF force field parameters were fitted to atomic coordinates, atomic charges, crystal cell parameters, and relative potential energies taken from either experimental measurements or high-fidelity calculations of the potential energy surface. We conducted an extensive set of quantum mechanical calculations on the materials involved in the reaction of titanium and boron. These calculations include single point energies as well as structural optimizations, with the goal of including the following in the training set:
1. Fully optimized unit cells
2. Unit cell compression and expansion
3. TiB_2 crystal vacancies
4. Gas phase PES studies
5. Snapshots of a periodic, layered Ti/B system undergoing reaction

Training Set Construction: Solid state density functional theory (DFT) calculations were conducted with the ABINIT plane wave code, with the exception of those pertaining to ωTi. This structure (for unknown reasons) proved difficult to model with plane waves, and was therefore modeled with localized (Gaussian-type) basis sets using the Crystal09 software. The PBE exchange-correlation functional was used for all calculations, and Trouiller-Martins-type pseudopotentials were used for all plane wave calculations. All reported energies were computed in $P1$ symmetry using a 12×12×12 Monkhorst-Pack (M-P) grid and a kinetic energy cutoff of either 30 au (for supercell structures) or 60 au (for single unit cells). Atomic charges were obtained from a Bader (atoms-in-molecules) post-processing analysis of the electron density. Single molecule studies were conducted with the Gaussian03 software, using the LANL2DZ basis set and effective core potentials. Periodic Car-Parrinello MD simulations were conducted with the NWChem pseudopotential plane wave code (E_{cutoff} = 20 au, 2x2x2 M-P grid for k point sampling).

Prior to the work reported here, there were no ReaxFF force field parameters or parameter training set for the reaction of Ti and B. Parameters existed for Ti and B individually, but not for their interaction. Much of the current effort was devoted to construction of a training set consisting of a representative set of atomic configurations and their associated energies and charge distributions. The training set includes the following bulk Ti, B, TiB, Ti_2B, and TiB_2 structures:

1. Ti: α (hcp), β (bcc), ω(hcp) phases, as well as simple cubic and fcc structures
2. B: the rhombohedral α and β phases, the high pressure orthorhombic γ phase, as well as simple cubic, fcc, bcc, and hcp structures
3. TiB: orthorhombic, bcc and hcp structures
4. Ti_2B: tetragonal structure
5. TiB_2: the highly stable hcp structure, as well as rhombohedral and tetragonal structures

The most stable crystal phases at room temperature and standard pressure are shown in Figure 47. The high pressure phases of Ti and B are the ω and γ phases, respectively. For all structures, the fully optimized unit cell structure (coordinates and cell parameters) and its energy was included in the training set. The cell parameters and relative energy per atom (E_{atom}) are listed for Ti and B in Tables V and VI, respectively. Tables VII-IX provide the cell parameters and formation energies (E_f) for the TiB, Ti_2B and TiB_2 stuctures. Many of the structures listed above are not known to be stable forms of the material and some were found to have very high energies. These structures are included in the training set in order to ensure the force field will properly predict their instabilities. The formation energies calculated for hcp TiB_2 (-3.00 eV) and orthorhombic TiB (-1.60 eV) are in good agreement with the experimental values of -2.90 eV and -1.66 eV, respectively.[50]
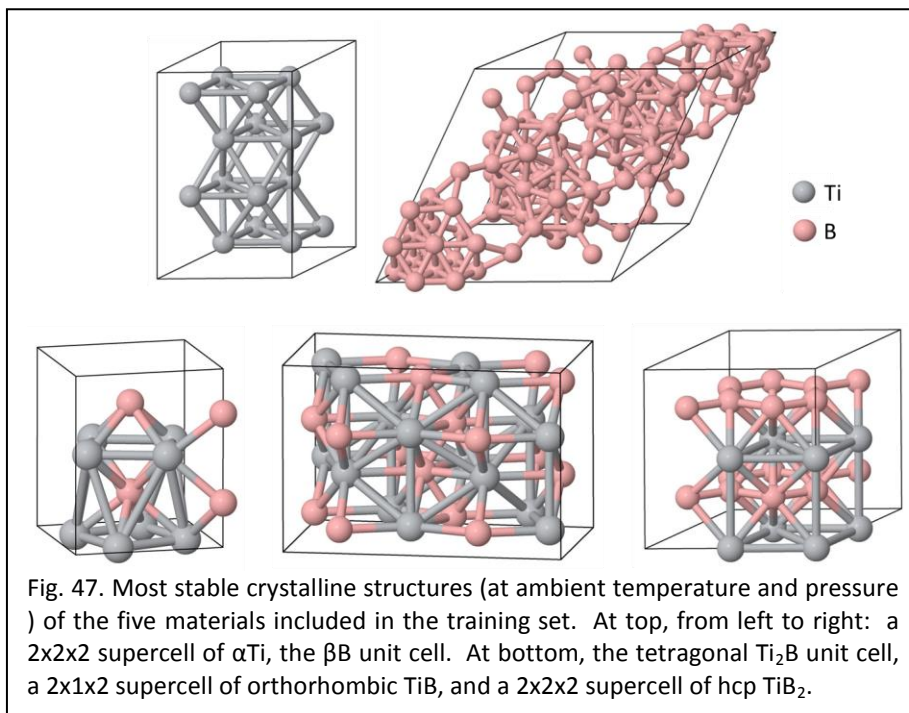

Fig. 47. Most stable crystalline structures (at ambient temperature and pressure) of the five materials included in the training set. At top, from left to right: a 2x2x2 supercell of αTi, the βB unit cell. At bottom, the tetragonal Ti_2B unit cell, a 2x1x2 supercell of orthorhombic TiB, and a 2x2x2 supercell of hcp TiB_2.

Table V Crystal phases of titanium.

Phase	Symmetry	N_{atoms} / uc	a	b	c	Density	E_{atom} (eV)
α	$P6_3/mmc$ (hcp)	2	3.053		4.524	4.368	0
β	$Im\bar{3}m$ (bcc)	2	3.349			4.233	0.098
ω*	$P6/mmm$ (hcp)	3	4.554		2.808	4.730	-0.010
	$Pm\bar{3}m$ (cubic)	1	3.042			2.824	0.832
	$Fm\bar{3}m$ (fcc)	4	4.192			4.316	-0.033

* high pressure phase

Table VI Crystal phases of boron.

Phase	Symmetry	N_{atoms} / uc	a	b	c	Density	E_{atom} (eV)
α [a]	$R\bar{3}m$ (rhomb.)	12	5.011			2.506	-0.134
β [b]	$R\bar{3}m$ (rhomb.)	111	10.139			2.428	0
γ*	$Pnnm$ (orthorhombic)	28	5.025	5.600	6.860	2.603	-0.106
	$Pm\bar{3}m$ (cubic)	1	2.067			2.034	1.582
	$Fm\bar{3}m$ (fcc)	4	2.919			2.886	1.257
	$Im\bar{3}m$ (bcc)	2	2.128			3.727	1.883
	$P6_3/mmc$ (hcp)	2	2.308		2.805	2.774	1.390

[a] symmetrized crystal, α = β = γ = 58.557°
[b] symmetrized crystal, α = β = γ = 66.013°
* high pressure phase

Table VII Crystal phases of titanium monoboride (TiB).

Symmetry	N_{atoms} / uc	a	b	c	Density	E_f (eV)
Pnma (orthorhombic)	8	4.577	6.160	3.107	4.451	-1.604
$Im\bar{3}m$ (bcc)	2	2.833			4.288	0.040
$P6_3/mmc$ (hcp)	2	2.697		4.315	3.586	1.225

Table VII Crystal phases of titanium semiboride (Ti$_2$B).

Symmetry	N_{atoms} / uc	a	b	c	Density	E_f (eV)
I4/mcm (tetragonal)	12	4.806		5.743	4.465	-1.299

Table VIII Crystal phases of titanium diboride (TiB_2).

Symmetry	N_{atoms} / uc	a	b	c	Density	E_f (eV)
$P6/mmm$ (hcp)	3	3.045		3.291	4.366	-2.997
$R\bar{3}m$ (rhomb.)	9	3.045		11.610	3.715	-1.243
$P4_2/mnm$ (rutile)	6	4.138		4.635	2.908	5.758

Compression/expansion (c/e) curves were computed for three Ti phases (α, β and ω), two B phases (α and γ) and hcp TiB_2. Cubic and uniaxial compression and expansion was computed from 50% compression to 20% expansion in increments of 0.05. Results are plotted in Figure 48.
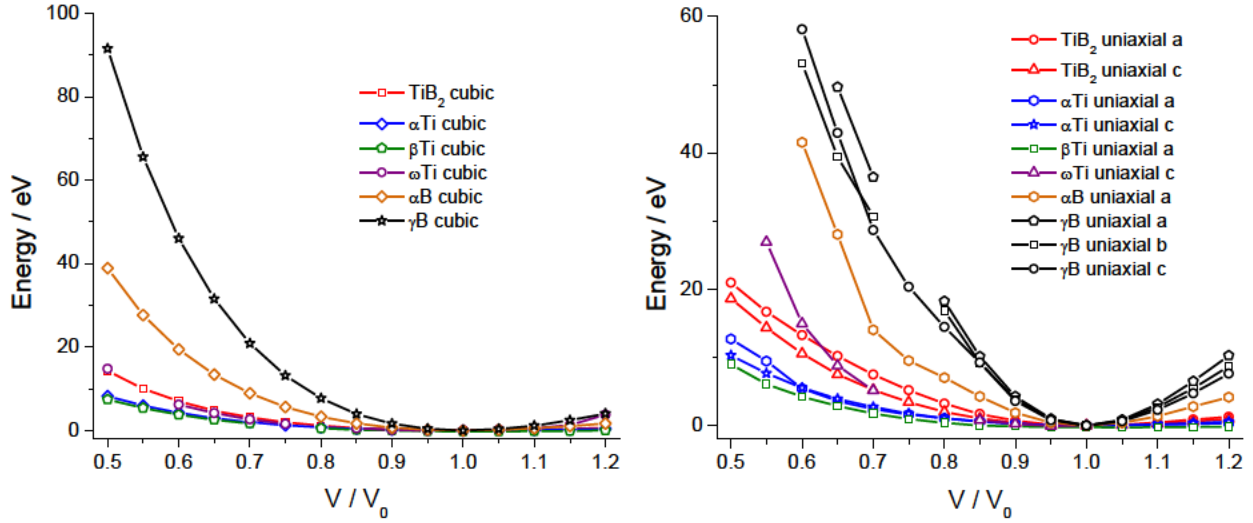
Fig. 48. Compression/expansion curves for Ti, B and TiB_2.

Vacancy energies were computed for removal of a single B or Ti atom from 2x2x2 and 3x3x3 supercells of hcp TiB_2. In these calculations the atomic coordinates of the defective crystal were relaxed with the cell parameters frozen at the values of the perfect crystal. The vacancy energy was computed according to the following equation

$$E_{Ti/B \, vac} = [E_{TiB_2}(N\text{-}1) + E_{Ti/B}] - E_{TiB_2}(N)$$

where $E_{TiB_2}(N\text{-}1)$ is the energy of the defective supercell, $E_{TiB_2}(N)$ the energy of the perfect supercell, and $E_{Ti/B}$ the energy per atom of Ti or B in the bulk material (α phase in both cases). Results are summarized in Table IX.

Table IX Titanium diboride (hcp) vacancy energies.

Supercell	Vacancy fraction	$E_{Ti \, vac}$ (eV)	$E_{B \, vac}$ (eV)
2x2x2	0.042	4.555	3.130
3x3x3	0.012	4.506	2.952

Although the MD studies we planned for the force field all involve condensed phase systems it is often useful to include work on gas phase systems in the training set. The main advantages with gas phase systems are they are often smaller and hence computationally cheaper to

46

model, and they can be used to make the bond stretch, angle and torsion terms of the ReaxFF potential form more straightforward to parameterize. An extensive examination of gas phase clusters containing only Ti and B yielded several stable potential energy minima. Unfortunately however the ground electronic states of these Ti-B clusters are rarely singlet spin, making their connection to the condensed phase system somewhat complicated. In an attempt to avoid this difficulty, we investigated a Ti-B cluster containing capping H atoms (TiB_4H_8). This compound has very weak Ti-B bonding however, and as a result the potential energy as a function of the B-Ti-B bond angle is effectively constant. Ultimately, we decided to study the potential energy surface of triplet (ground state) Ti_2B_6, and include these results (summarized in Figures 49 and 50) in the training set. This compound has similarities in structure to the TiB_2 crystal: six boron atoms in a hexagonal ring with Ti atoms on either side of the plane, forming a line that intersects the centroid of the hexagon. The spin density resides on the Ti atoms. The B-B and Ti-Ti bonds are shorter (by 0.16 and 0.l9 Å, respectively) and stronger than those of the optimized crystal, because the atomic coordination numbers are significantly lower in the cluster. On the other hand, the Ti-B distances (2.19 Å) are very similar to those of the crystal (2.20 Å).
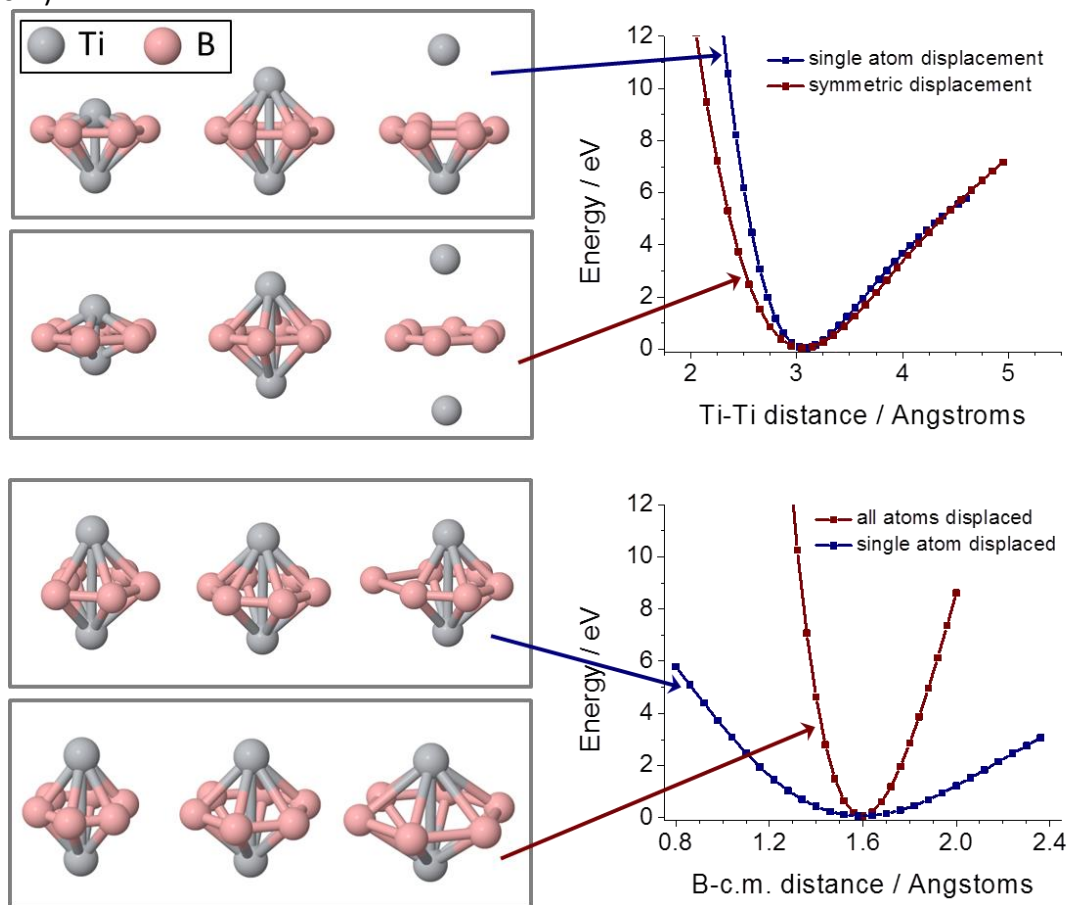

Fig. 49. Potential energy surface scans of the triplet Ti_2B_6 cluster. The graph at the top shows the energy as a function of Ti-Ti distance. The bottom plot graphs the energy as function distance of the boron atom(s) from the midpoint of the Ti-Ti bond vector, which is the center of mass when the cluster is in perfect symmetry.
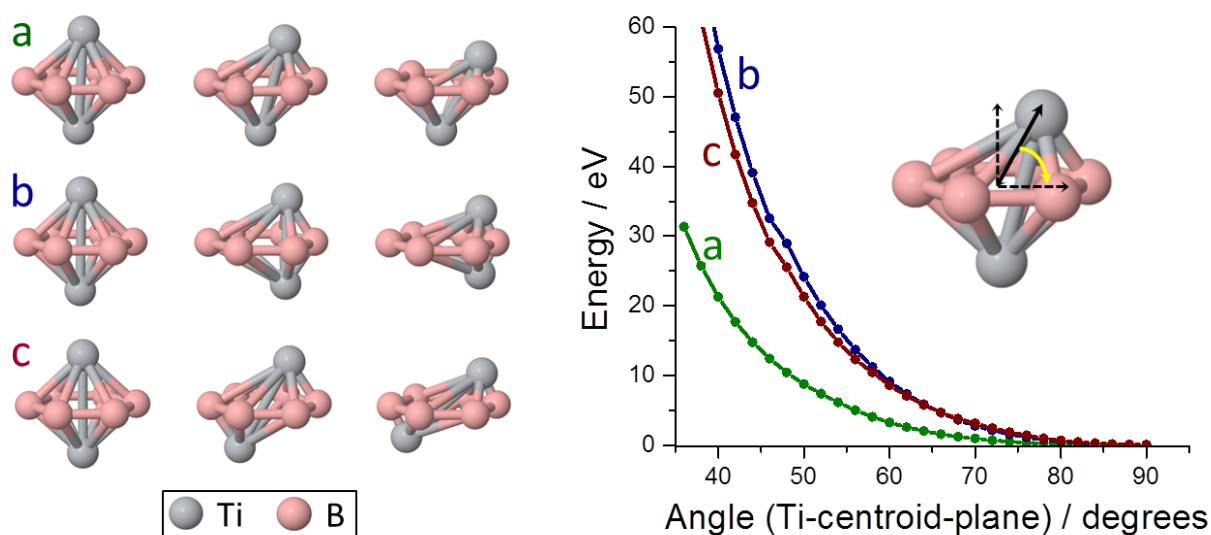
47

Fig. 50. Potential energy surface scans of the triplet Ti_2B_6 cluster. The energy is plotted as a function of the angle between the Ti atom(s), the centroid of the B hexagon, and the plane of the B atoms. For curve a, only one of the Ti atoms is displaced, and for curves b and c, both are displaced by the same angle.

Condensed phase MD sampling: Finally, we performed a high-temperature Car-Parrinello MD simulation in order to produce amorphous structures to use for both force field training and validation. First, a layered Ti/B system was constructed from 2½ unit cells of αTi (12 atoms) and a single unit cell γB (28 atoms). The cell parameters and atomic coordinates of the system were then optimized using ABINIT (2×2×2 M-P grid, 20 au energy cutoff). The resulting structure is shown in the far left of Figure 51, doubled along _a_, _b_ and _c_, to give a better view. During the MD simulation, the system evolved from zero temperature to 3000 K using a Nosé-Hoover thermostat with a time constant of 0.24 ps. The volume of the simulation cell was kept fixed throughout. Snapshots of the system along the trajectory are shown in Figure 51. The atomic coordinates, cell parameters, relative energies, and atomic charges for each of these snapshots were included in the training set for force field parameterization.
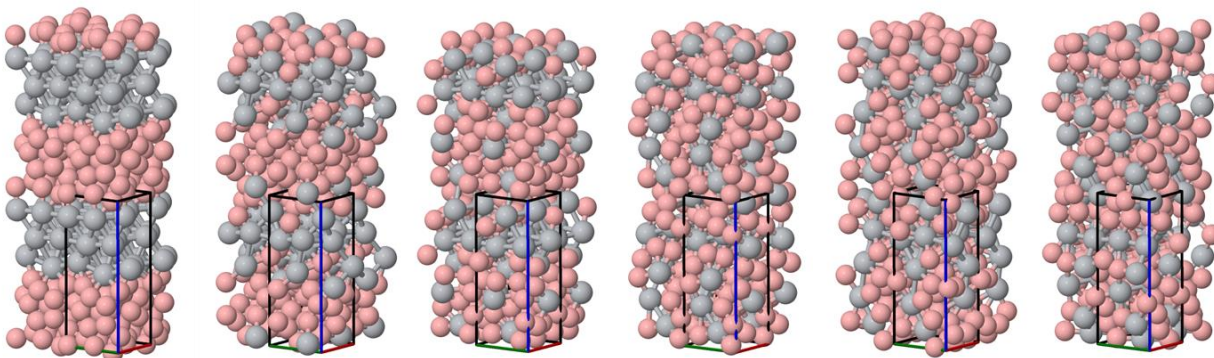

Fig. 51. Snapshots of periodic, layered Ti/B system undergoing thermally-induced chemical reaction. The original simulation cell (outlined in red, green, blue and black lines) was doubled in each dimension for visualization clarity.

ReaxFF Parameter Optimization: Training set consists of more than 300 atomic configurations, representing both single molecule and condensed phase structures, with associated energies and charge distributions. Training the ReaxFF potential to accurately describe the solid state chemistry of Ti and B involves optimization of 78 force field parameters, describing Coulombic interactions as well as bond stretching, bending and torsion. Parameter optimization is achieved through minimization of a cost function using a single parameter search algorithm. In general, an adequately parameterized force field is obtained through proper description of the reference properties (the training set) as well as proper weighting of these properties in the cost function. For example, though the training set consists of approximately 300 atomic configurations and their associated properties (e.g., potential energies), some of these configurations (particularly those at or near an energy minimum) are more important than others. In the energy cost function, the structures should be weighted according to their "relative importance." Determining the relative importance of each data in the training set is challenging, and unfortunately, thus far our optimization attempts have yielded unsatisfactory results. Work is ongoing, and the training set data is available upon request.

BIBLIOGRAPHY

[1] N.N. Thadhani et al (Eds), Multifunctional Energetic Materials; MRS. Proc.,896, 2005; p 123.

[2] N. N. Thadhani: *J Appl Phys*, 1994, **76**, 2129-2138.

[3] S. S. Batsanov, G. S. Doronin, S. V. Klochkov: *Fizika Goreniya i Vzryva*, 1987, **22**, 765-768.

[4] D.E. Eakins and NN. Thadhani, International Materials Reviews, August 2009.

[5] Y. Horie and M. E. Kipp: *J Appl Phys*, 1988, **63**, 5718-5727; **84**, 1292-1298 and 3574-3580.

[6] I. Do and D. J. Benson: Int. J. Plasticity, 2001, **17**, 641-668; International Journal of Computational Engineering Science, 2000, **1**, 61-79.

[7] M. Baer, Thermochimica Acta **384**, 351-367 (2002).

[8] S.H. Fisher and M.C. Grubelich, 32ndAIAA/ASME/SAE/ASEE Jointt Propulsion conference, Lake Buena Vista, FL, July 1-3, 1996, SANDIA Report SAND95-2448C.

[9] A.J. Gavens, D. Heerdan, A. Mann, E. Reiss, T.P. Weihs, J. Appl. Phys., 87(3), (2000), 1255.

[10] N.N. Thadhani, R.A. Graham, T. Royal, M. U. Anderson, *J. Appl. Phys.*, **82**, (1997), p.1113.

[11] X. Xu and N. N. Thadhani: *J Appl Phys*, 2004, **96**, 2000.

[12] D. E. Eakins and N. N. Thadhani: *J Appl Phys*, 2006, **100**, 113521.

[13] D.Eakins and N.N. Thadhani, Appl. Phys. Letts., 92 (2008) 111903

[14] B. R. Krueger, A. H. Mutz, and T. Vreeland Jr.: *Metall. Transactions A*, 1992, **23A**, 55-58.

[15] A. Al-Omari and E. Masad, Int. J. Numer. Analyt. Meth. Geomech. **28**, 1327 _2004.

[16] A. D. Jadhav, N. P. Padture, E. H. Jordan, M. Gell, E. R. Fuller, Jr., Acta Mater. **54**, 3343 2006.

[17] Wulf J, Steinkopff T, Fischmeister HF. Acta Mater, 1996;44(5):1765.

[18] Zhai J, Tomar V, Zhou M. J Eng Mater Tech 2004;126:179–91.

[19] S. D. Bona, L. Lutzemberger, and O. Salvetti, Phys. Med. Biol. **48**, 4001, (2003).

[20] T. Kanit, et al, Comp. Meth. App. Mech. Eng. **195**, 3960 (2006).

[21] Benson D, Conley P. Model Simulat Mater Sci Eng 1999;7:333–54.

[22] D. Benson, Raven – A Multimaterial Eulerian Hydrocode, ver. 1.09; February 2006.

[23] D. J. Benson, W. Tong, and G. Ravichandran, Modell. Simul. Mater. Sci. Eng. **3**, 771 (1995).

[24] D. Eakins and N.N. Thadhani, Journal of Applied Physics, 2007, Vol. 101 (200) 043508-18.

[25] D.E. Eakins and N.N.Thadhani, Acta Materialia, 56 (2008) pp. 1496-1510.

[26] B. Aydellotte and N.N. Thadhani, to be presented at JANNAF Conf, San Diego, Dec 2009.

[27] H. Singh and A. M. Gokhale: Materials Characterization, Vol. 54, No. 1, PP 21-29, 2005.

[28] S. I. Lieberman, A. M. Gokhale, S. Tamirisakandala, D. B. Miracle, J. Metals,59(1), 2007, p59.

[29] S.I. Lieberman, A.M. Gokhale, S. Tamirisakandala, R.B. Bhat: Mat. Charac., 60, (2009) 957.

[30] H. Singh, Y. Mao, and A.M. Gokhale: Mod. & Sim. in Matls. Sci. & Eng., 14, (2006) P 351.

[31] H. Singh, A.M. Gokhale, Y. Mao, J. E. Spowart:, Acta Mater., 54(8), PP 2131-2143, 2006.

[32] Y. Mao, A.M. Gokhale, and J. Harris: Comp. Matls Sci., Vol. 37, Issue 4, PP 543-556, 2006.

[33] Z. Shan and A.M. Gokhale: Acta Materialia,Vol. 49, PP. 2001-2015, 2001.

[34] A. Gokhale, H. Singh, Z. Shan: Comp. Methods, eds., G. R. Liu et al. Springer, (2005) P 1629.

[35] G. Saheli, H. Garmestani, A. M. Gokhale: Int. J. of Phys. & Mech. Sol. 3(1) PP 85-107, 2008.

[36] R. T. DeHoff and F. N. Rhines, Quantitative Microscopy, McGraw-Hill, New York, NY, 1968.

[37] A. M. Gokhale: "Quantitative Characterization and Representation of Global Microstructural Geometry," ASM Handbook, eds. G. F. Vander Voort, Vol. 9, PP 428-447, 2004.

[38] A. Tewari, A.M. Gokhale, J. E. Spowart, D. B. Miracle: Acta Mater., 52(2), PP. 307-319, 2004.

50

[39] H. Singh, A. M. Gokhale, et al., Matls. Sci. & Eng, 474(1-2), P 104-111, 2008.

[40] D. Stoyan, S. Kendall, J. Mecke, Stochastic Geometry and its App., John Wiley, NY, 1995.

[41] A. Tewari, A.M. Gokhale, and R.M. German: Acta Materialia, Vol. 47, PP. 3721-3734, 1999.

[42] T. Royal, S. Namjoshi, and N.N. Thadhani, Metall. & Matls. Trans., 27A, 1761-1771, (1996).

[43] Shankar M R, Chandrasekar S, King A H and Compton W D 2005 *Acta Mater.* **5** 4781-93.

[44] Fredenburg D A, Vogler T J, Saldana C J and Thadhani N N 2007 *AIP Conf. Proc.* **955** 1029-32

[45] Gonzales, M. Gurumurthy, A. Kennedy, G. B. Gokhale, A. M. and Thadhani, N. N. 2013. MRS Proceedings. 1521.

[46] P. Specht, N.N. Thadhani, and T. Weihs, "Configurational Effects on Shock Wave Propagation in Ni-Al Multilayer Composites," J.l of App. Phys., Vol. 111 (7), 2012.

[47] G. P. Purja Pun and Y. Mishin, *Phil. Mag. B*, 89, 1 (2009).

[48] S. Zhao, T. C. Germann, and A. Strachan, *Phys. Rev. B*, 76, 14103 (2007).

[49] A. V. Bolesta, L. Zheng, D. L. Thompson and T. D. Sewell, Phys. Rev. B 76, 224108 (2007).

[50] Chase, M.W., Jr., NIST-JANAF Themochemical Tables, Fourth Edition, *J. Phys. Chem. Ref. Data*, Monograph 9, 1998, 1-1951.

DEPARTMENT OF DEFENSE

DEFENSE THREAT REDUCTION
AGENCY
8725 JOHN J. KINGMAN ROAD
STOP 6201
FORT BELVOIR, VA 22060
      ATTN: S. PEIRIS

DEFENSE TECHNICAL
INFORMATION CENTER
8725 JOHN J. KINGMAN ROAD,
SUITE 0944
FT. BELVOIR, VA 22060-6201
      ATTN: DTIC/OCA

**DEPARTMENT OF DEFENSE
CONTRACTORS**

QUANTERION SOLUTIONS, INC.
1680 TEXAS STREET, SE
KIRTLAND AFB, NM 87117-5669
      ATTN: DTRIAC